

# African hydroclimate during the early Eocene from the DeepMIP simulations

Charles J. R. Williams<sup>1,2</sup>, Daniel J. Lunt<sup>1</sup>, Ulrich Salzmann<sup>3</sup>, Tammo Reichgelt<sup>4</sup>,  
Gordon N. Inglis<sup>5</sup>, David R. Greenwood<sup>6</sup>, Wing-Le Chan<sup>7</sup>, Ayako Abe-Ouchi<sup>7</sup>, Yannick  
Donnadieu<sup>8</sup>, David K. Hutchinson<sup>9,10</sup>, Agatha M. de Boer<sup>9</sup>, Jean-Baptiste Ladant<sup>11</sup>,  
Polina A. Morozova<sup>12</sup>, Igor Niezgodzki<sup>13,14</sup>, Gregor Knorr<sup>14</sup>, Sebastian Steinig<sup>1</sup>,  
Zhongshi Zhang<sup>15</sup>, Jiang Zhu<sup>16</sup>, Matthew Huber<sup>17</sup>, Bette L. Otto-Bliesner<sup>16</sup>

<sup>1</sup>School of Geographical Sciences, University of Bristol, UK

<sup>2</sup>NCAS / Department of Meteorology, University of Reading, UK

<sup>3</sup>Geography and Environmental Sciences, Northumbria University, UK

<sup>4</sup>Department of Geosciences, University of Connecticut, USA

<sup>5</sup>School of Ocean and Earth Science, University of Southampton, UK

<sup>6</sup>Department of Biology, Brandon University, Canada

<sup>7</sup>Atmosphere and Ocean Research Institute, The University of Tokyo, Japan

<sup>8</sup>Centre Européen de Recherche et d'Enseignement des Géosciences de l'Environnement,  
France

<sup>9</sup>Department of Geological Sciences, Stockholm University, Sweden

<sup>10</sup>Climate Change Research Centre, University of New South Wales, Australia

<sup>11</sup>Laboratoire des Sciences du Climat et de l'Environnement, France

<sup>12</sup>Institute of Geography, Russian Academy of Sciences, Russia

<sup>13</sup>Institute of Geological Sciences, Polish Academy of Sciences, Poland

<sup>14</sup>Alfred Wegener Institute for Polar and Marine Research, Germany

<sup>15</sup>Bjerknes Centre for Climate Research, University of Bergen, Norway

<sup>16</sup>Climate and Global Dynamics Laboratory, National Center for Atmospheric Research, USA

<sup>17</sup>Department of Earth, Atmospheric and Planetary Sciences, Purdue University, USA

**Corresponding author address:** School of Geographical Sciences, University Road, Bristol, BS8  
1SS, UK

**Email:** c.j.r.williams@bristol.ac.uk

**Short title:** Early Eocene simulations of African hydroclimate

**Keywords:** Palaeoclimate, DeepMIP, Early Eocene, African precipitation



## KEY POINTS

- 1) State-of-the-art climate models are used to study African hydroclimate during the early Eocene (approximately 50 million years ago).
- 2) With increasing levels of CO<sub>2</sub>, there are changes to African precipitation, due to dynamical changes such as low level circulation.
- 3) A comparison between the models and newly-compiled climate estimates shows a marginally better match at lower levels of CO<sub>2</sub>.

## ABSTRACT

The early Eocene (~56-48 million years ago) is characterised by high CO<sub>2</sub> estimates (1200-2500 ppmv) and elevated global temperatures (~10 to 16°C higher than modern). However, the response of the hydrological cycle during the early Eocene is poorly constrained, especially in regions with sparse data coverage (e.g. Africa). Here we present a study of African hydroclimate during the early Eocene, as simulated by an ensemble of state-of-the-art climate models in the Deep-time Model Intercomparison Project (DeepMIP). A comparison between the DeepMIP pre-industrial simulations and modern observations suggests that model biases are model- and geographically dependent, however these biases are reduced in the model ensemble mean. A comparison between the Eocene simulations and the pre-industrial suggests that there is no obvious wetting or drying trend as the CO<sub>2</sub> increases. The results suggest that changes to the land sea mask (relative to modern) in the models may be responsible for the simulated increases in precipitation to the north of Eocene Africa. There is an increase in precipitation over equatorial and West Africa and associated drying over northern Africa as CO<sub>2</sub> rises. There are also important dynamical changes, with evidence that anticyclonic low-level circulation is replaced by increased south-westerly flow at high CO<sub>2</sub> levels. Lastly, a model-data comparison using newly-compiled quantitative climate estimates from palaeobotanical proxy data suggests a marginally better fit with the reconstructions at lower levels of CO<sub>2</sub>.

## PLAIN LANGUAGE SUMMARY

Approximately 50 million years ago, a period known as the early Eocene, atmospheric carbon dioxide levels were significantly higher than today, and were more similar to what they could be in the future, if efforts to reduce human greenhouse gas emissions are unsuccessful. However, rainfall changes during this period are less well understood, especially over data-sparse regions such as Africa. Here, a collection of state-of-the-art climate models are used to study African rainfall during this period, comparing the simulations firstly to present-day African rainfall (to validate the models), secondly to varying levels of atmospheric carbon dioxide, and lastly to newly-compiled reconstructions of early Eocene rainfall (from plant fossils). The main findings are that although the models can reproduce present-day rainfall over Africa, and compare reasonably well with the reconstructions, there is no clear rainfall signal when atmospheric carbon dioxide is increased. Nevertheless, the combination of a

73 different continental configuration, vegetation, topography and atmospheric carbon dioxide leads to  
74 changing rainfall patterns, connected to temperature and low level wind changes.  
75

## 1. INTRODUCTION

One of the ways to better understand future anthropogenic-induced climate change is to simulate past climates, using these as partial analogues for the future and allowing the testing of climate models to simulate climates very different from today (Braconnot *et al.* 2011, Tierney *et al.* 2020). Simulating past climates allows not only an interrogation of the mechanisms of past climate change (Haywood *et al.* 2020, Lunt *et al.* 2021), but if a robust comparison with available proxy data can be produced, this allows confidence in future climate change projections that are often based on models tuned to a modern climate state (Harrison *et al.* 2014, Taylor *et al.* 2011, Williams *et al.* 2020, Williams *et al.* 2021, Zhu *et al.* 2020).

It has long been known that African precipitation, and in particular that over West Africa, is of vital importance to the more than one billion people in sub-Saharan Africa who survive predominantly on rain-fed agriculture and, concurrently, are highly vulnerable to extreme precipitation events causing both flooding and drought (Williams and Kniveton 2011). However, a lack of weather and climate data across much of the continent has resulted in a high level of uncertainty concerning both present day and future climate trends (Salerno *et al.* 2019), and although it is expected that both average temperature and precipitation will increase across Africa along with the rest of the world (IPCC 2021), regional variation is particularly high across Africa.

Due to their particular relevance to African precipitation, two Quaternary time periods have recently been investigated by Williams *et al.* (2020) under the Palaeoclimate Modelling Intercomparison Project (PMIP, Braconnot *et al.* 2007), now in its 4<sup>th</sup> phase and itself under the umbrella of the Coupled Model Intercomparison Project, now in its 6<sup>th</sup> phase (CMIP6, Eyring *et al.* 2016). These time periods are the mid-Holocene (6000 years ago, 6 ka) and Last Interglacial (127 ka). However, excess warmth and enhancement of the Northern Hemisphere during these periods is caused primarily by changes to the orbital configuration of Earth, rather than elevated greenhouse gases (Kageyama *et al.* 2018). To investigate substantial greenhouse gas-induced warming, and its result on regional hydroclimate such as across Africa, periods further back in time are needed, and two such candidates in the context of PMIP are the mid-Pliocene (~3 million years ago, 3 Ma) and the early Eocene (~56.05-47.8 Ma). However, with CO<sub>2</sub> levels ranging from 316-420 ppmv during the mid-Pliocene (Martínez-Botí *et al.* 2015), this is more similar to modern levels rather than being a suitable analogue for future projections by the end of the 21<sup>st</sup> century; using the previous RCP 8.5 scenario, this could be over 1000 ppmv (IPCC 2013). The early Eocene, with CO<sub>2</sub> levels ranging between 1200-2500 ppmv (Anagnostou *et al.* 2016, Anagnostou *et al.* 2020, Lunt *et al.* 2021), is comparable to the current future projections, and in particular for the extended high-emissions/low-mitigation scenarios such as in the year 2300 under SSP5-8.5 (Arias *et al.* 2021). As a result of this high CO<sub>2</sub>, the early Eocene was a period characterised by temperatures up to ~5°C higher than today in the tropics (e.g. Cramwinckel *et*

*al.* 2018, Gaskell *et al.* 2022, Inglis *et al.* 2020, Pearson and Wade 2007), and much greater polar amplification with temperatures reaching ~20°C warmer than today at terrestrial high latitudes (e.g. Huber and Caballero 2011, Naafs *et al.* 2018, van Dijk *et al.* 2020).

Despite being a partial analogue for future climate change, until the last few years climate model simulations of high CO<sub>2</sub> periods such as the early Eocene have not been evaluated within a consistent framework (Lunt *et al.* 2017); the closest to this was an informal model-data comparison, considering four climate models, known as the Eocene Model Intercomparison Project (EoMIP), undertaken by Lunt *et al.* (2012). This work focused on temperature-based metrics, however another study by Carmichael *et al.* (2016) used the same EoMIP ensemble to look at the hydrological cycle and hydroclimate changes in response to the elevated CO<sub>2</sub> levels in the early Eocene. The results focusing specifically on Africa are discussed in more detail below but, globally, when compared to proxy data it was found that the models generally underestimated precipitation over high latitudes, and those models showing the most warming in these regions gave the best match to the data (Carmichael *et al.* 2016). Concerning the impact of elevated CO<sub>2</sub>, it was found that all early Eocene simulations showed a more intense hydrological cycle (relative to the pre-industrial era, hereafter PI), with enhanced global precipitation and evaporation, and that this was generally directly related to the elevated temperatures resulting from higher CO<sub>2</sub> (Carmichael *et al.* 2016). At any given level of CO<sub>2</sub>, global precipitation changes varied widely between models, and certain regions (such as tropical Africa, discussed further below) were found to be sensitive to which model was assessed (Carmichael *et al.* 2016).

However, a disadvantage (albeit unavoidable) to EoMIP was that there was no consistent framework to the models' experimental design; each used different boundary conditions (e.g. palaeogeography) and different levels of CO<sub>2</sub> (Lunt *et al.* 2012). To resolve this problem, therefore, more recently the Deep Time Model Intercomparison Project (DeepMIP) was envisaged and conducted, using CMIP3 and CMIP5 models as well as some of the most recent state-of-the-art CMIP6-class models (Lunt *et al.* 2017). The large-scale features coming out of the simulations are discussed in Lunt *et al.* (2021), with several conclusions being drawn. Firstly, boundary conditions other than CO<sub>2</sub>, discussed in Section 2.1, contributed between 3-5°C of the global mean early Eocene warming, relative to the PI (Lunt *et al.* 2021). Secondly, the DeepMIP simulations showed less of a temperature spread than the models in EoMIP, and an increase in climate sensitivity (Lunt *et al.* 2021). Lastly, when compared to proxy SST data, most models reproduced the large-scale spatial patterns of the reconstructions but still struggled at the regional scale, such as in the south-west Pacific (Lunt *et al.* 2021).

Similar to Lunt *et al.* (2012), Lunt *et al.* (2021) only focused on temperature and CO<sub>2</sub>-based metrics. The majority of recent studies looking at Eocene hydroclimate have focused on reconstructing

evidence for the Asian monsoon (e.g. Farnsworth *et al.* 2019, Ma *et al.* 2019, Licht *et al.* 2014, Quan *et al.* 2012, Xie *et al.* 2019). There are very few studies, and in particular modelling studies, focusing on Africa. The aforementioned study by Carmichael *et al.* (2016) using the EoMIP ensemble found that tropical Africa was particularly sensitive to the model in question, and that the models varied in skill (when reproducing precipitation, relative to observations) in regions of relatively low precipitation such as over northern Africa's Sahel region. Moreover, although some models showed similar PI precipitation over tropical Africa, under early Eocene conditions they were quite different (Carmichael *et al.* 2016). It should be noted, however, that this study did not actually include any early Eocene mean annual precipitation (MAP) reconstructions from Africa, only some Lutetian samples (~41-47 Ma). More recently, Carmichael *et al.* (2018) ran several CO<sub>2</sub> simulations using just the UK Met Office Hadley Centre model HadCM3L, finding an increase in both the size and frequency of extreme precipitation events over equatorial and East Africa. Although MAP changes were relatively small, extreme rainfall increased by up to 70% over parts of tropical Africa, with summer precipitation events dominating the regime over southern Africa (Carmichael *et al.* 2018). Another example of Eocene African work is that of Liu *et al.* (2019), who looked at the Asian, African and Australian monsoons across five different time periods and found that precipitation from the African monsoon existed as early as the mid-Paleocene. Keery *et al.* (2018) found the variability of Asian and African precipitation during the Eocene was predominantly accounted for by orbital configuration changes such as the precession and obliquity; in DeepMIP, however, these were kept at PI values and so, here, the impact on African precipitation will only be down to the CO<sub>2</sub> or the other boundary condition changes.

In this paper four main questions are addressed:

- 1) How well do the DeepMIP models' PI simulations reproduce modern observations of African precipitation?
- 2) What is the impact of CO<sub>2</sub> and other early Eocene boundary conditions on African precipitation in the DeepMIP models' early Eocene simulations?
- 3) What are the physical mechanisms behind this precipitation response?
- 4) How do the DeepMIP models' early Eocene simulations compare with proxy data of African precipitation?

Section 2 of this paper briefly describes the experimental design followed by the DeepMIP models, gives a brief introduction to the models themselves, and describes the observational and proxy data used for comparative purposes. Section 3 presents the results, addressing each of the above questions. Section 4 summarises and concludes.

## 2. EXPERIMENT DESIGN, MODELS, AND PROXY DATA

## 2.1. Experiment design

The full experimental design, which all DeepMIP modelling groups were required to follow as closely as possible, is detailed extensively in Lunt *et al.* (2017) and so will only be briefly outlined here. In addition to the various CO<sub>2</sub> experiments, all modelling groups were required to carry out a PI simulation for comparison purposes, which was to be as close as possible to the CMIP6 standard *piControl* simulation (Eyring *et al.* 2016).

For the early Eocene simulations, a number of boundary conditions needed to be changed, the key ones for the African region of which are shown in Figure 1.

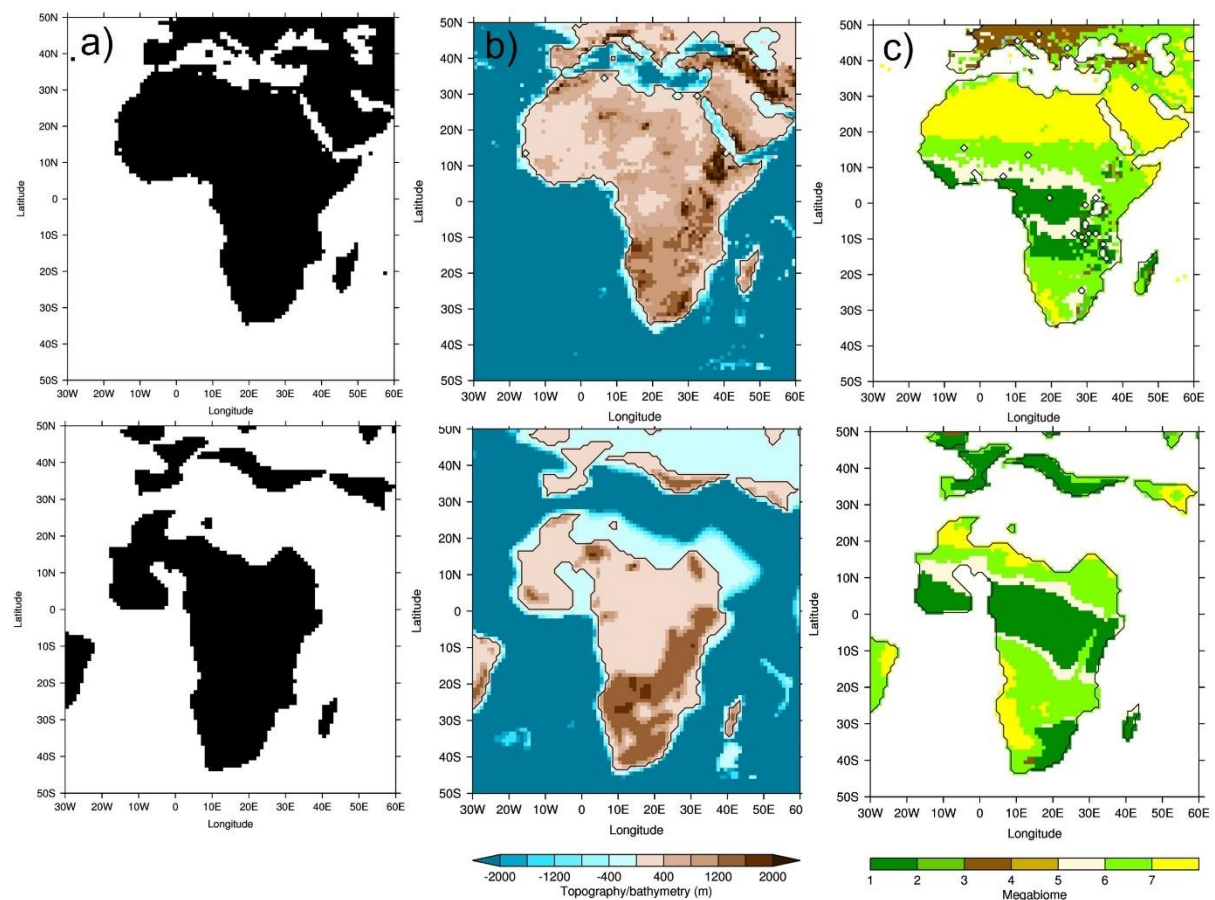


Figure 1 – Main boundary conditions changed in DeepMIP simulations, where top row = PI and bottom row = early Eocene: a) Land sea mask; b) Topography/bathymetry; c) Vegetation, expressed as megabiomes according to Harrison and Prentice (2003) (where 1 = Tropical, 2 = Warm-temperate, 3 = Temperate, 4 = Boreal, 5 = Savanna, 6 = Grassland and 7 = Desert). The PI topography/bathymetry is taken from ETOPO5, re-gridded to 1°x1° resolution, whereas the other fields are from Herold *et al.* (2014)

Firstly, the land sea mask (LSM) was based on the palaeogeographic heights (discussed further below), with possible manual manipulation required in some models to maintain the various gateways (Lunt *et al.* 2017). The new LSM produced a geographically smaller Africa relative to the PI, with



much of the present-day landmass north of 20°N being ocean in the early Eocene due to the increased sea level (Figure 1a). Secondly, the palaeogeography (including topography and bathymetry) was based on the digital reconstruction of the early Eocene from Herold *et al.* (2014), with the topography (and sub-grid scale topography) being applied as an absolute value rather than as an anomaly (Lunt *et al.* 2017). Over Africa, the most pronounced changes were over southern and eastern Africa, with generally larger areas of raised topography in the early Eocene, relative to the PI (Figure 1b). This can be seen more clearly in the Supplementary Material, where the differences in topography are shown; there is clearly a large increase in elevation over western Africa where there is land in the early Eocene but ocean in the PI, but apart from this (where the landmasses coincide) the largest changes are over southern and eastern Africa (Figure S1). Thirdly, concerning the land surface, vegetation and river run-off routing was also based on the dataset of Herold *et al.* (2014), using an appropriate lookup table to convert the vegetation megabiomes into whatever format was required by the model (Lunt *et al.* 2017). The early Eocene vegetation was created by running the dynamic vegetation model BIOME4 (Kaplan *et al.* 2003), with the resulting 27 biomes being consolidated into 10 megabiomes following the procedure of Harrison and Prentice (2003); please see Table 3 in Harrison and Prentice (2003) for a distinction between these megabiomes. BIOME4 itself was forced by Eocene topography, bathymetry and CO<sub>2</sub> coming out of an early Eocene simulation from the CESM climate model. Concerning how well the simulated vegetation compares with reconstructions, Herold *et al.* (2014) state that it compares well with vegetation inferred from Palaeocene and Eocene palynoflora (Utescher and Mosbrugger 2007, Morley 2007), and is consistent with geological indicators of climate (Crowley 2012). Although Herold *et al.* (2014) highlight a dry bias in vegetation over South America, there is no specific mention of Africa, primarily because there is currently little or no palaeobotanical data for Africa, meaning validation was not possible. Although it is beyond the scope of this study to modify the vegetation boundary conditions, previous work has suggested a high sensitivity to vegetation, showing for example dramatically increased global annual mean temperatures when interactive vegetation is used, compared to fixed vegetation (Loftson *et al.* 2014).

When compared to the PI, over Africa the new vegetation resulted in: i) a loss of the desert regions over the present-day Sahara, primarily because this is ocean in the early Eocene; ii) a latitudinal expansion (relative to the PI) of tropical rainforest across central Africa; and iii) an addition of a large area of tropical rainforest over southern Africa, which is savanna or grassland in the PI (Figure 1c). However, some features remained similar in the early Eocene relative to the PI, such as the region of tropical rainforest across central Africa being bordered by savannah to the north and south, and the Namib Desert (Figure 1c). The impact on precipitation of these three boundary condition changes is discussed below. Soil parameters, including soil dust fields, were given a globally constant value, and (given the lack of palaeodata) no lakes were prescribed unless dynamically predicted (Lunt *et al.* 2017). Concerning greenhouse gas concentrations, the CO<sub>2</sub> experiments were divided into a set of

standard experiments (which all modelling groups should ideally have conducted) and a set of sensitivity experiments (which were optional). All of these were expressed as multiples of the PI simulation, typically with a CO<sub>2</sub> of 280 ppmv, and were as follows: 3x and 6x the PI for the standard experiments, and 1x, 1.5x, 2x, 4x and 9x the PI for the sensitivity experiments (Lunt *et al.* 2017). See Table 1 for which modelling groups conducted which experiments. All other greenhouse gases were kept as PI, the justification for which is given in Lunt *et al.* (2017). Concerning aerosols, given the rapid development of representation of aerosols in models the experimental design was flexible here and allowed modelling groups to either leave these as PI, treat aerosols interactively (if possible), prescribe aerosols from Herold *et al.* (2014), or a combination of the above (Lunt *et al.* 2017). The solar constant and astronomical parameters were kept identical to the PI, the justification for which is again given in Lunt *et al.* (2017).

Modelling group responsible	Model	Atmospheric resolution (lon x lat)	CO <sub>2</sub> experiments undertaken	Run length (years)	References
University of Michigan, US	CESM1.2_CAM5	2.5° x 1.89°	1x, 3x, 6x, 9x	2000	Hurrell <i>et al.</i> (2013)
Alfred Wegener Institute, Germany / Polish Academy of Sciences, Poland	COSMOS-landveg_r2413	3.75° x 3.71°	1x, 3x, 4x	9500	Jungclaus <i>et al.</i> (2006)
Stockholm University, Sweden	GFDL_CM2.1	3.75° x 3.05°	1x, 2x, 3x, 4x, 6x	6000	Delworth <i>et al.</i> (2006)
University of Bristol, UK	HadCM3B_M2.1aN	3.75° x 2.5°	1x, 2x, 3x	7800	Valdes <i>et al.</i> (2017)
University of Bristol, UK	HadCM3BL_M2.1aN	3.75° x 2.5°	1x, 2x, 3x	7800	Valdes <i>et al.</i> (2017)
National Academy of Sciences, Russia	INM-CM4-8	2° x 1.5°	6x	1050	Volodin <i>et al.</i> (2018)
Laboratoire des Sciences du Climat et de l'Environnement, France	IPSLCM5A2	3.75° x 1.89°	1.5x, 3x	4000	Sepulchre <i>et al.</i> (2020)
University of Tokyo, Japan	MIROC4m	2.8125° x 2.79°	1x, 2x, 3x	5000	Chan <i>et al.</i> (2011)
University of Bergen, Norway	NorESM1_F	2.5° x 1.89°	2x, 4x	2100	Guo <i>et al.</i> (2019)

Table 1 - Models taking part in DeepMIP, including relevant details and references

Lastly, the experimental design provided some advice on practical matters such as simulation length and output format. The simulations varied in length (see Table 1) but were all at least 1000 years in length, with the climatologies, comprising the results discussed here, being calculated over the final 100 years. At that point, all simulations should have had a global mean top-of-the-atmosphere (TOA) net radiation balance of less than  $0.3 \text{ W m}^{-2}$  (or a similar balance to that of the PI) and an SST trend of less than  $0.1^{\circ}\text{C century}^{-1}$  (Lunt *et al.* 2017). All of the output, details of which are given in Lunt *et al.* (2017), were uploaded to a centralised DeepMIP database.

## 2.2. Models

Extensive details on each model, and how the experimental design was implemented in their simulations, are given in Lunt *et al.* (2021) and references therein and will therefore only briefly be discussed here; those aspects likely to affect precipitation (e.g. convection and land-surface schemes) will be focused upon here. In total, nine models were included in DeepMIP, although it should be noted that two of these are different configurations of the same model. See Table 1 for a list of the models, along with their atmospheric spatial resolutions and appropriate references (particularly relating to the atmospheric component of the models and elements relating to hydroclimate, where available). In detail, these are as follows.

- CESM1.2\_CAM5: The Community Earth System Model version 1.2 (CESM1.2) is comprised of the Community Atmosphere Model version 5.3 (CAM5), the Community Land Model version 4.0, the Community Ice Code version 4.0 and the Parallel Ocean Program version 2 (Hurrell *et al.* 2013). CAM5 uses the finite-volume dynamical core and physical parameterizations of deep convection (Zhang and McFarlane 1995), shallow convection and moist turbulence (Park and Bretherton 2009), and cloud microphysics (Morrison and Gettelman 2008). This version contains new physical parameterisations in the atmosphere, such as the cloud microphysics, which is critical for the simulation of the large-scale climate features of the early Eocene (Liu *et al.* 2017)
- COSMOS-landveg\_r2413: For an atmospheric general circulation model, ECHAM5 (the European Centre Hamburg Model) is used (Roeckner *et al.* 2003), and this is coupled to the Max-Planck-Institute for Meteorology Ocean Model (MPIOM) (Marsland *et al.* 2003); the coupled model is described by Jungclaus *et al.* (2006). COSMOS-landveg\_r2413 simulates cumulus convection using a mass flux scheme. The orography is represented in spectral domain by surface geopotential (see Stepanek and Lohmann 2012 for more details regarding model description). The land surface conditions for each biome are based on Hagemann (2002); additionally, parameters with a seasonal cycle (i.e. leaf area index and vegetation ratio) in the latitude belt of  $\sim 20^{\circ}\text{S}$ - $20^{\circ}\text{N}$  were smoothed and an annual average for each biome was prescribed.

- 296 • GFDL\_CM2.1: This uses the Geophysical Fluid Dynamics Laboratory (GFDL) CM2.1 model  
297 (Delworth *et al.* 2006), with modifications as described in Hutchinson *et al.* (2018), and  
298 comprising the Atmosphere Model 2, Land Model 2 and the Sea Ice Simulator 1, coupled to  
299 the ocean component from the modular ocean model version 5.1 (MOM5.1). The atmosphere  
300 uses a finite-volume discretisation, and a 3° latitude x 3.75° longitude resolution with 24  
301 vertical levels, following the configuration of CM2Mc (Galbraith *et al.* 2011). Convection is  
302 parameterised by the relaxed Arakawa-Schubert scheme of Moorthi and Suarez (1992), with a  
303 lower-bound on entrainment as specified in Tokioka *et al.* (1988). Cloud microphysics are  
304 parameterised using the scheme of Rotstayn (1997), while cloud macrophysics use the  
305 parameterisation of Tiedtke (1993). Full details of the convection and cloud  
306 parameterisations are given in Delworth *et al.* (2006). Of possible relevance to the simulation  
307 of precipitation, the topography is smoothed using a three-point mean filter to allow a  
308 smoother interaction with the wind field (Lunt *et al.* 2021).
- 309 • HadCM3B\_M2.1aN: This Hadley Centre Climate Model (HadCM3) version is documented  
310 extensively in Valdes *et al.* (2017). In particular, the model uses a single ‘bulk’ cloud model  
311 to parameterise dry as well as shallow and deep moist convection (Grant 1998). The cloud  
312 scheme uses a statistical parametrization via a probability density function over the grid-box  
313 total water content (Bushell 1998). Six short-wave and eight long-wave radiation bands are  
314 represented by the scheme of Edwards and Slingo (1996). Static fields for the nine surface  
315 types of the MOSES2.1 land surface scheme (Cox *et al.* 1999) are derived from the ten  
316 megabiomes of the DeepMIP vegetation boundary conditions (Herold *et al.* 2014) via a  
317 lookup table. The atmosphere uses a Cartesian grid with a horizontal resolution of 3.75 x 2.5°  
318 (longitude x latitude) and 19 hybrid vertical levels.
- 319 • HadCM3BL\_M2.1aN: The only difference between this version of HadCM3 and the one  
320 described above is the horizontal resolution of the ocean component (Cox 1984), at 1.25° x  
321 1.25° for HadCM3B\_M2.1aN and 3.75° x 2.5° for HadCM3BL\_M2.1aN, and associated  
322 diffusion parameters (Valdes *et al.* 2017). Both versions use 20 unequally spaced vertical  
323 levels in the ocean ranging between 10 and 616 m.
- 324 • INM-CM4-8: This version of the Institute of Numerical Mathematics (INM) model is  
325 described in Volodin *et al.* (2018), but the parameterisations of physical processes are the  
326 same as in the previous version, INM-CM5, and described more detail in Volodin *et al.*  
327 (2017). Parameterization of condensation and cloud formation follows Tiedtke (1993), and  
328 cloud water is a prognostic variable. Parameterization of cloud fraction follows Smagorinsky  
329 (1963); cloud fraction is a diagnostic variable, independent of the calculation of condensation,  
330 and depended on the relative humidity. Deep and shallow convection is parameterized by  
331 Bets (1986). The surface, soil and vegetation scheme follow Volodin and Lykossov (1998),

with the evolution of the equations for temperature, soil water and soil ice being solved at 23 levels from the surface to 10 meters depth (Volodin *et al.* 2018). The fractional area of 13 types of potential vegetation is specified, and actual vegetation as well as LAI is calculated according to the soil water content in the root zone and soil temperature (Volodin *et al.* 2018).

- IPSLCM5A2: The IPSL-CM5A2 Earth system model from the Institut Pierre Simon Laplace (IPSL) is documented by Sepulchre *et al.* (2020), and is based on the previous generation IPSL Earth system model (IPSLCM5A, Dufresne *et al.* 2013) but with new revisions such as a re-tuning of global temperature. It comprises the LMDZ5 (Laboratoire de Météorologie Dynamique Zoom) atmosphere model, the Organising Carbon and Hydrology In Dynamic Ecosystems (ORCHIDEE) land surface and vegetation model and the Nucleus for European Modeling of the Ocean (NEMOv3.6) ocean model, which includes the LIM2 sea ice model and the Pelagic Interactions Scheme for Carbon and Ecosystem Studies (PISCESv2) biogeochemical model (Lunt *et al.* 2021). LMDZ5 runs at a horizontal resolution of  $1.9^\circ \times 2.5^\circ$  (latitude  $\times$  longitude) with 39 hybrid sigma-pressure levels. The LMDZ5 radiation scheme is inherited from the European Center for Medium-Range Weather Forecasts (Fouquart and Bonnel 1980, Morcrette *et al.* 1986), and the dynamical effects of the subgrid-scale orography are parameterized according to Lott (1999). Turbulent transport in the planetary boundary layer is treated as a vertical eddy diffusion (Laval *et al.* 1981), with counter-gradient correction and dry convective adjustment, and the surface boundary layer is treated according to Louis (1979). Cloud cover and cloud water content are computed using a statistical scheme (Bony and Emanuel 2001). For deep convection, the LMDZ5A version uses the “episodic mixing and buoyancy sorting” scheme originally developed by Emanuel (1991).
- MIROC4m: This version of the Model for Interdisciplinary Research on Climate (MIROC) is documented by K-1 model developers (2004) and summarized in Chan *et al.* (2011). In the atmosphere model, cumulus parameterization is based on Arakawa and Schubert (1974), with some simplifications and the cloud base mass flux is treated as a prognostic variable. Cumulus convection is suppressed when the cloud-mean ambient relative humidity is less than the critical value of 0.8. The land surface model (Minimal Advanced Treatments of Surface Interaction and Runoff, MATSIRO) is documented by Takata *et al.* (2003), where prognostic variables include canopy temperature, canopy water content, snow amount, soil moisture content and frozen soil moisture content. Fixed vegetation types are specified over ice-sheet-free. The ocean component is version 3.4 of the CCSR (Center for Climate System Research) Ocean Component Model (COCO), documented in Hasumi (2000).
- NorESM1\_F: This version of the Norwegian Earth System Model (NorESM) is described in detail in Guo *et al.* (2019) and Li *et al.* (2020), and differs from the previous version

(NorESM1-M) in that while it has the same atmosphere-land grid, the ocean and sea ice components use a tripolar grid (rather than the bipolar grid in NorESM1-M), resulting in a more realistic Atlantic Meridional Overturning Circulation (Lunt *et al.* 2021). NorESM1\_F couples the Miami Isopycnic Coordinate Ocean Model (MICOM) and the spectral Community Atmosphere Model (CAM4) (Eaton 2010, Neale *et al.* 2008, Neale *et al.* 2013). CAM4 includes the Zhang and McFarlane (1995) deep convection scheme, the Hack (1994) shallow convection scheme, the nonlocal boundary layer scheme of Holtslag and Boville (1993) and the representation of cloud microphysics and macrophysics by Rasch and Kristjánsson (1998) and Zhang *et al.* (2003). Instead of using the undiluted convective available potential energy (CAPE) in the original deep convection scheme, the diluted CAPE through an explicit representation of entrainment has been used to close the cumulus parameterization (Neale *et al.* 2008). The convective momentum transport has also been included in the parameterization of deep convection (Richter and Rasch 2008). Additionally, NorESM1\_F adopts energy updates and energy conservation. Compared to NorESM1-M, NorESM1\_F has several important improvements on how precipitation is simulated, such as improvements in seasonality, a reduced wet bias and mitigation of the common double intertropical convergence zone (ITCZ) problem (Li *et al.* 2020).

### 2.3. Observational and proxy data

Here the observational and proxy data are described; firstly there is a description of the modern, satellite-derived data used to assess and evaluate the PI simulations, and secondly there is a description of the early Eocene proxy data used to evaluate the Eocene simulations.

#### 2.3.1. Satellite-derived rainfall estimates from the modern period

Even in the 21<sup>st</sup> century, there is a severe lack of in-situ rain gauge data over Africa; South Africa is probably the best populated in terms of rainfall measurements, but in other countries such as Angola or Namibia rain gauge data are sparse or non-existent (e.g. Williams *et al.* 2007, Williams *et al.* 2008, Williams *et al.* 2010). The CenTrends precipitation dataset (Funk *et al.* 2015) contains measurements going back to 1900, but only for a small number of countries in East Africa. Likewise, although the Global Historical Climate Network (GHCN) database (Durre *et al.* 2008, Durre *et al.* 2010, Menne *et al.* 2012) does contain temperature measurements going back to 1861, precipitation measurements do not begin until the 1950s and are again relatively sparse in Africa. Therefore, a possible solution to the problem of data unavailability is to use satellite-derived rainfall estimates (SREs), which offer near-uniform coverage at relatively high spatial resolution from the 1980s onwards.

Several datasets of SREs currently exist, but here the Tropical Applications of Meteorology using SATellite data and ground-based observations (TAMSAT) is used. TAMSAT (version 3.1) provides

daily, 10-daily, monthly and seasonal precipitation estimates over Africa at 4 km resolution, and extends from 1983 to the present-day. The data are publicly available; please see Open Research section, and Maidment *et al.* (2014), Maidment *et al.* (2017) and Tarnavsky *et al.* (2014) for details. Here, TAMSAT is used as a comparative tool for evaluating the PI simulations of the DeepMIP models. A caveat here is that the models are showing precipitation simulated under PI boundary conditions, whereas TAMSAT is showing precipitation from the late 20<sup>th</sup> and early 21<sup>st</sup> century (referred to here as modern) and will therefore contain an anthropogenic signal; this, however, is unavoidable given the lack of PI precipitation observations. It is expected that the biases between comparing the models to PI precipitation versus comparing them to modern precipitation will be less than the biases between the models themselves (i.e. the inter-model spread), and indeed much less than the uncertainty associated with the Eocene reconstructions.

### 2.3.2. *Palaeobotanical Eocene precipitation estimates*

The distribution and physiognomy of land plants are sensitive to precipitation (Wright *et al.* 2017). Therefore, the taxonomic affinity and the morphology of leaf fossils can be used to generate palaeo-precipitation estimates (e.g. Utescher *et al.* 2014, Wilf *et al.* 1998). For this study, previously established Paleocene-Eocene (~41-56 Ma) palaeobotanical records from Africa were compiled (see Supplementary Material for age ranges for individual sites, Table S1). The distribution of the nearest living relatives (NLR) of these taxa was then analyzed using the bioclimatic analysis approach to find the highest probability precipitation range in which all taxa could co-occur (e.g. West *et al.* 2020, Willard *et al.* 2019).

Geodetic coordinates of occurrences were obtained for the NLR of each plant group from the Global Biodiversity Information Facility (GBIF) (see Supplementary Material, Table S2). These occurrence datasets were then filtered for uncertain, exotic and superfluous occurrences, as well as subjected to a random resampling to avoid regional overrepresentation of densely sampled areas. A climatic envelope for each plant group (see Table S2) was then generated by extracting precipitation data (mean annual precipitation (MAP), wettest month (WMP), driest month (DMP), warmest and coldest quarter precipitation (WQP and CQP, respectively) and the precipitation seasonality coefficient (PS)) using the DISMO package in R (Hijmans *et al.* 2005). A probability density function was then generated for each co-occurring plant group by testing the likelihood of the plant group occurring at 100,000 unique extant combination of MAP, WMP, DMP, PS, WQP and CQP. As shown in Equation 1, the product of probabilities ( $f$ ) was calculated for each plant group ( $t$ ) at each climatic combination ( $x$ ), using the means ( $\mu$ ) and standard deviations ( $\sigma$ ) of their modern-day bioclimatic envelope, for each climatic variable ( $c$ ).

$$f(t_n) = \prod_{i=1}^6 \frac{1}{\sqrt{2\sigma_c^2} \times \pi} e^{x_c - \mu_c / 2\sigma_c^2}$$

Equation 1

A combined likelihood for all plant groups in the assemblage combined can then be calculated with the product of all likelihoods (n), shown in Equation 2.

$$f(z) = \prod_{i=1}^n t_n$$

Equation 2

The combination of MAP, WMP, DMP, PS, WQP and CQP with the highest likelihood is the value reported here as most representative for the assemblage, and the highest and lowest values of the metrics with  $f(z) \geq 5\%$  of the maximum  $f(z)$  is represented as the uncertainty (using the 95% confidence interval).

Eleven plant assemblages from South Africa, Tanzania, South Sudan, Cameroon, Côte d'Ivoire, Ghana and Nigeria were analyzed with the bioclimatic analysis NLR method (Adeonipekun *et al.* 2012, Atta-Peters and Salami 2004, Cantrill *et al.* 2013, Chiaghanam *et al.* 2017, de Villiers 1997, Eisawi and Schrank 2008, Goha *et al.* 2016, Okeke and Umeji 2016, Salami 1984, Salard-Chebouldaef 1979, Uzodimma 2013); see Table S1 for age ranges of individual sites.

The NLR generated precipitation values were supplemented with an additional value based on leaf area analysis (LAA) derived data by Jacobs and Herendeen (2004) and Kaiser *et al.* (2006), also from Tanzania (from the Lutetian). In locations where the final results are in the same geographical location, the reconstructions were averaged. The final results of this analysis are shown in Table 2, with Eocene MAP expressed as ranges and modern MAP taken from TAMSAT. It should be noted that, for the results other than the model-data comparison, precipitation during June-August (JJA) is focused upon, rather than using MAP. Previous work has suggested that for much of the continent, over 80% of the annual total of precipitation is accounted for by a given region's wet season and, over West Africa (the wet season of which is JJA), this increases to 95% or higher (Liebmann *et al.* 2012). Given that the primary driver of this wet season is the seasonal progression of the ITCZ, it is likely that this relationship will hold during the early Eocene. It was therefore deemed appropriate to focus on this season for the majority of the analysis (i.e. Sections 3.1, 3.2 and 3.3), only using MAP for the model-data comparison (Section 3.4), for which seasonal proxy data are not available.



Site name	Latitude (°N)	Longitude (°E)	MAP (mm year <sup>-1</sup> )	
			Early Eocene	Modern
Koningsnaas, South Africa	-30.2	17.3	1318-1738	101
Shagamu, Nigeria	6.7	3.7	1148-2089	1762
Melut Basin, South Sudan	10	33	1175-1905	757
Kwakwa, Cameroon	4.5	9.1	1175-1905	2524
Mwadui, Tanzania	-3.9	33.5	813-1738	754
Tano, Ghana	4.7	-3	1514-2344	-
Nanka, Nigeria	6.12	7	1380-2291	1683
Abidjan margin, Côte d'Ivoire	5	-4.1	1660-1950	-
Okigwe, Nigeria	5.82	7.34	1175-1862	2311
Bende - Umuahia, Nigeria	5.47	7.45	1514-2291	2311
Araromi, Nigeria	7.7	3.5	1072-1738	1179
Mahenge, Tanzania	-4.79	34.26	720-800	707
Mahenge, Tanzania	-4.79	34.26	630-690	707
Mahenge, Tanzania	-4.79	34.26	737-815	707
Mahenge, Tanzania	-4.79	34.26	644-708	707
Mahenge, Tanzania	-4.79	34.26	710-790	707
Mahenge, Tanzania	-4.79	34.26	610-680	707
Mahenge, Tanzania	-4.79	34.26	610-680	707
Mahenge, Tanzania	-4.79	34.26	740-820	707

Table 2 - Locations and mean annual precipitation (MAP) from early Eocene palaeobotanical records from Africa, and modern values. Early Eocene ranges of MAP are expressed as the 95% confidence interval for all locations except Mahenge, where ranges are expressed as +/- 1 standard deviation. Modern values of MAP taken from TAMSAT; missing values indicate ocean regions, as TAMSAT MAP is land only

### 3. RESULTS

Here the results of different comparisons are described: i) a model validation exercise, where the models' PI simulations are compared to modern observations (Section 3.1); ii) a simulation

comparison, where precipitation from the models' early Eocene simulations, at varying levels of CO<sub>2</sub>, is compared (Section 3.2); iii) a simulation comparison, where the physical mechanisms behind the precipitation response are investigated (Section 3.3); and iv) a model-data comparison, where precipitation from the models' early Eocene simulations is compared to available proxy data (Section 3.4).

### **3.1. DeepMIP models' preindustrial simulations versus modern observations**

Here the focus is on mean precipitation differences between the various DeepMIP PI simulations (including the multi-model ensemble mean, MME) and precipitation observations from TAMSAT (see Section 2.3.1). Here, the MME is calculated for a given variable as the simple mean across all available models. Precipitation anomalies (PI simulations - TAMSAT) during JJA are shown in Figure 2, where the models have been ordered according to the root mean square error (RMSE), relative to TAMSAT. Two observations are noteworthy. Firstly, the MME is showing by far the closest agreement to TAMSAT, with a much lower RMSE (by ~10 mm month<sup>-1</sup> less than even the next lowest individual model), highlighting the importance of using the MME to counterbalance individual models' biases (whether they be under or overestimating). The MME will therefore subsequently be used when discussing the various Eocene simulations. Secondly, there appears to be a divide between: a) models such as IPSLCM5A2, INM-CM4-8 and COSMOS-landveg\_r2413 that are underestimating African precipitation (i.e. are showing drier conditions across West Africa at ~10°N), which have relatively low RMS error compared with TAMSAT; and b) models such as HadCM3BL\_M2.1aN, MIROC4m and GFDL\_CM2.1 that are overestimating African precipitation, which have relatively high RMS error compared with TAMSAT. For example, the model with the least agreement (GFDL\_CM2.1, RMSE = 70.6 mm month<sup>-1</sup>) is overestimating precipitation over West Africa by more than 100 mm month<sup>-1</sup>.

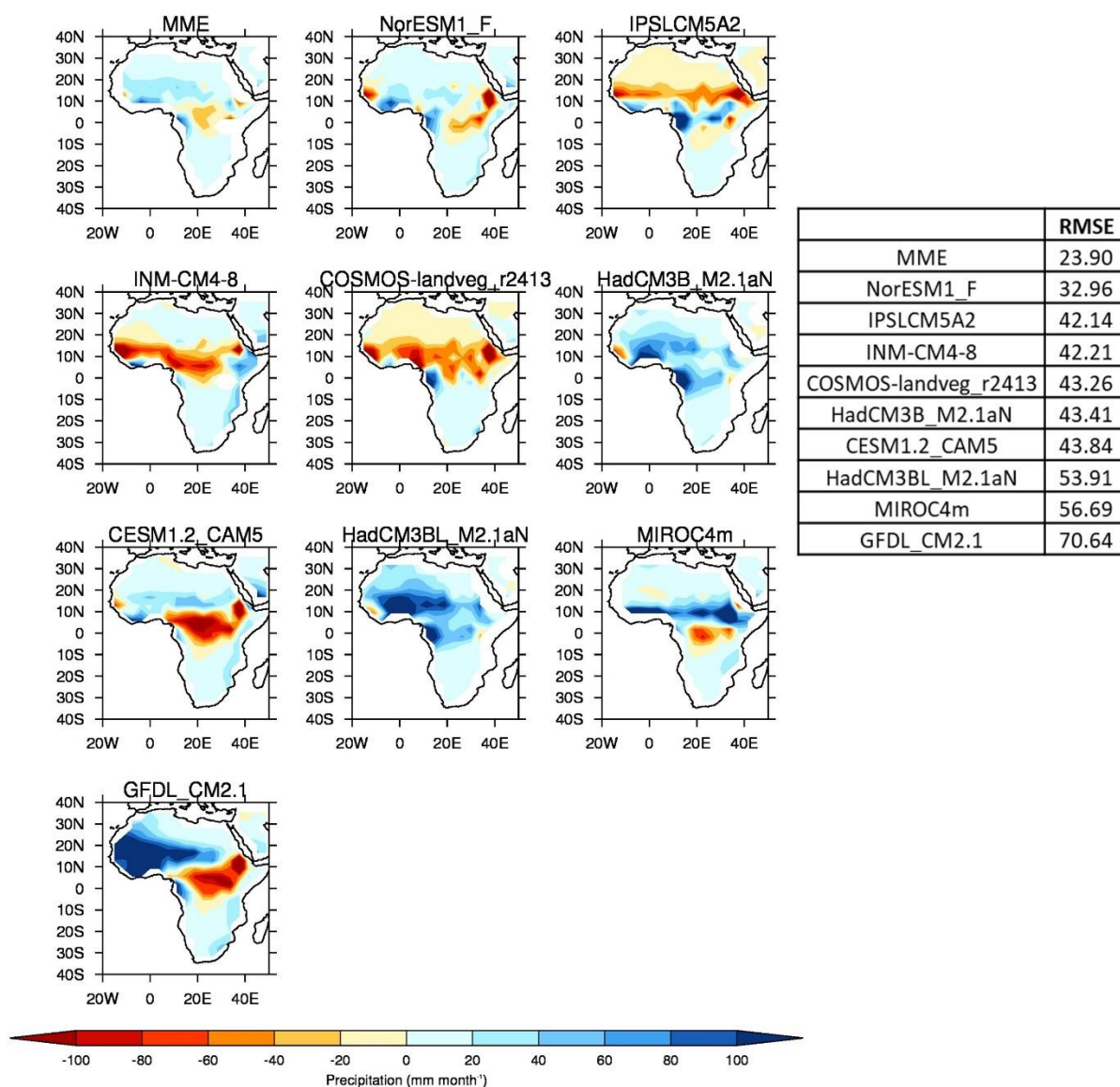


Figure 2 - JJA precipitation climatology differences (PI simulations - TAMSAT), re-gridded to lowest common spatial resolution (that of COSMOS-landveg\_r2413) and ordered according to Root Mean Squared Error (RMSE, in  $\text{mm month}^{-1}$ , see insert). RMSE calculated over  $20^{\circ}\text{W}$ - $50^{\circ}\text{E}$ ,  $40^{\circ}\text{N}$ - $40^{\circ}\text{S}$ , land points only

Concerning the seasonal and latitudinal distribution of African precipitation, Figure 3 shows the annual cycle of West African (defined here as land points only encompassing  $20^{\circ}\text{W}$ - $15^{\circ}\text{E}$ ,  $0$ - $20^{\circ}\text{N}$ ) precipitation and the zonal mean of JJA West African precipitation (Figure 3a and b, respectively). Outside of JJA, the majority of models are overestimating precipitation throughout the year (Figure 3a), with the model closest to TAMSAT (in terms of the seasonal cycle i.e. precipitation timings) being CESM1.2\_CAM5, although even this model overestimates precipitation during the first half of the year. When averaged over this region, only one model (INM-CM4-8) underestimates precipitation throughout the year, but is nevertheless closer to TAMSAT than those which overestimate, in agreement with that discussed above and shown in Figure 2. One model

(GFDL\_CM2.1) greatly overestimates precipitation especially during JJA, and others (such as INM-CM4-8) underestimate precipitation during JJA and therefore do not correctly reproduce the strong seasonality (i.e. the precipitation curve is flatter); for example, the difference between the wettest and driest month in this model is 136 mm month<sup>-1</sup>, whereas it is 161 mm month<sup>-1</sup> in TAMSAT and 181 mm month<sup>-1</sup> in the MME (Figure 3a). The MME also overestimates precipitation throughout the year but is nevertheless closer to TAMSAT in terms of seasonality than many of the wetter models (Figure 3a). Latitudinally, most models are showing a much wider (in terms of latitudinal extent) rain belt relative to TAMSAT, with GFDL\_CM2.1 and the HadCM3 family in particular not reproducing the observed rapid drop-off in precipitation either near the Equator or north of 15°N (Figure 3b). In part due to some drier models approaching the Equator (such as CESM1.2\_CAM5 and INM-CM4-8), the MME is showing a similar latitudinal extent of precipitation compared to TAMSAT, and while it is still too wet at low latitudes it does correctly drop off north of 15°N (Figure 3b).

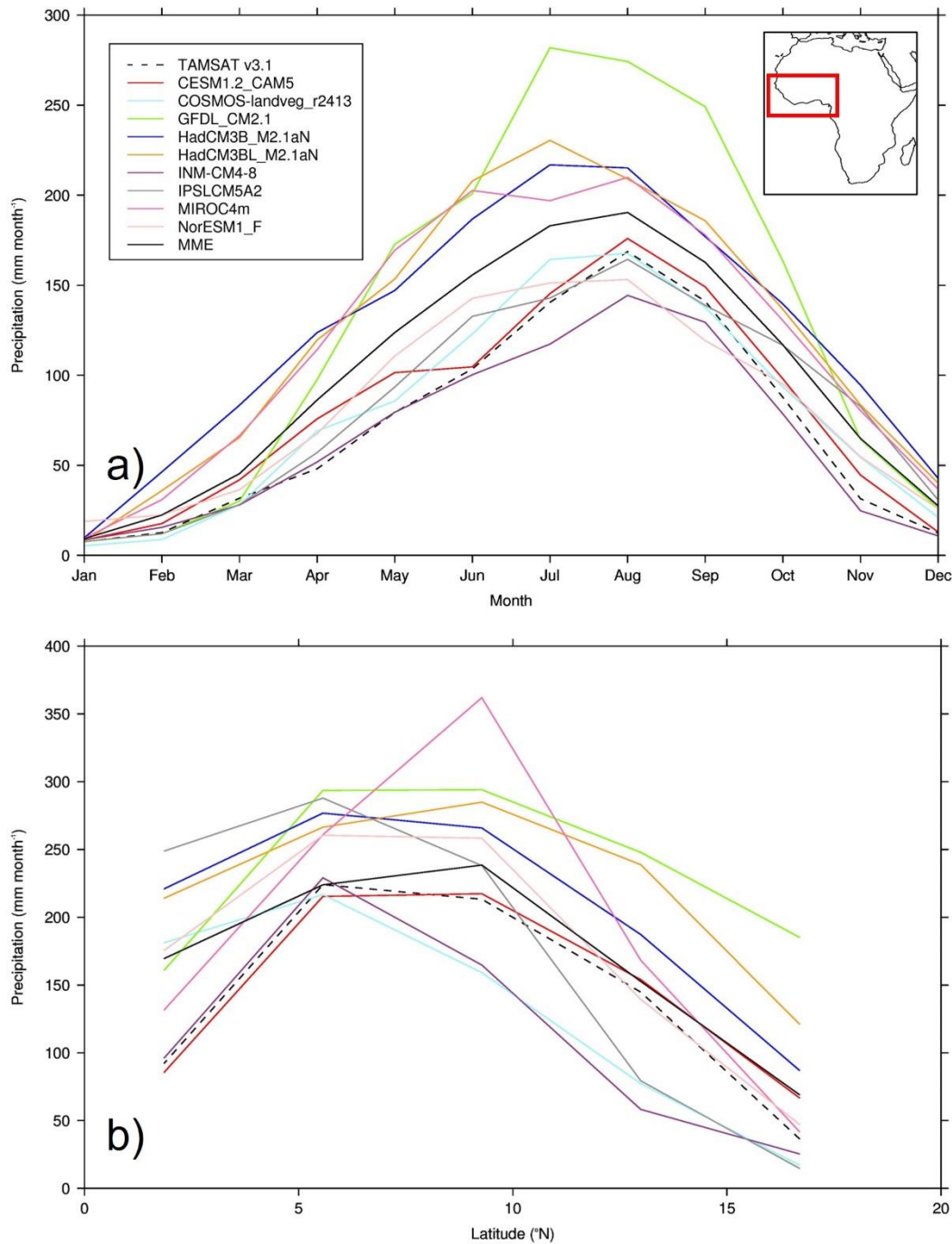


Figure 3 - Precipitation climatology from TAMSAT and PI simulations, averaged over West Africa (20°W-15°E, 0-20°N - land points only): a) Mean seasonal cycle, at each model's individual spatial resolution; b) Zonal mean of JJA precipitation, re-gridded to lowest common spatial resolution

### 3.2. DeepMIP models' early Eocene simulations relative to preindustrial simulations and each other

Here the focus is on mean precipitation differences between various DeepMIP early Eocene CO<sub>2</sub> sensitivity experiments, in which all boundary conditions other than CO<sub>2</sub> were kept identical. The focus is not only on the precipitation response to varying CO<sub>2</sub> concentrations relative to the PI

simulations, but also from each CO<sub>2</sub> experiment individually (relative to each other). Precipitation anomalies of all the CO<sub>2</sub> experiments versus PI are firstly briefly presented (Section 3.2.1), and then the experiment results are divided into a CO<sub>2</sub> component (Section 3.2.2) and a non-CO<sub>2</sub> component (i.e. the impact of the other boundary condition changes, Section 3.2.3).

Before these results are presented, however, a brief introduction to the early Eocene precipitation over Africa is needed. Mean JJA precipitation over PI and early Eocene Africa (using the 1x CO<sub>2</sub> simulation) is shown in the Supplementary Material, where it is clear that, during the PI, all models are showing a band of precipitation between approximately the Equator and 10°N that extends from the central equatorial Atlantic all the way across Africa (Figure S2a). How far east this rainbelt extends is dependent on model, but the majority (and the MME) show it extending up to 40°E. During the early Eocene, although this rain belt is still present over West Africa, most models agree that it does not extend across the continent, instead ending at ~20°E and being replaced by relatively drier conditions (Figure S2b). Wetter conditions are shown further east, over the early Eocene Indian Ocean, but concerning Africa these results would suggest that although the rain belt is latitudinally similar to the PI, it does not have the longitudinal extent.

### ***3.2.1. All CO<sub>2</sub> experiments versus preindustrial***

The precipitation anomalies (early Eocene - PI), for each CO<sub>2</sub> experiment and for each model during JJA are shown in Figure 4. This is only briefly presented, because the combination of a palaeogeographic forcing and a CO<sub>2</sub> forcing makes interpretation difficult; this is why the results are broken down into a CO<sub>2</sub> component and non-CO<sub>2</sub> component below. It should be noted that when the MME is discussed below (see Sections 3.2.2 and 3.2.3), only models that participated in the particular experiment are included.

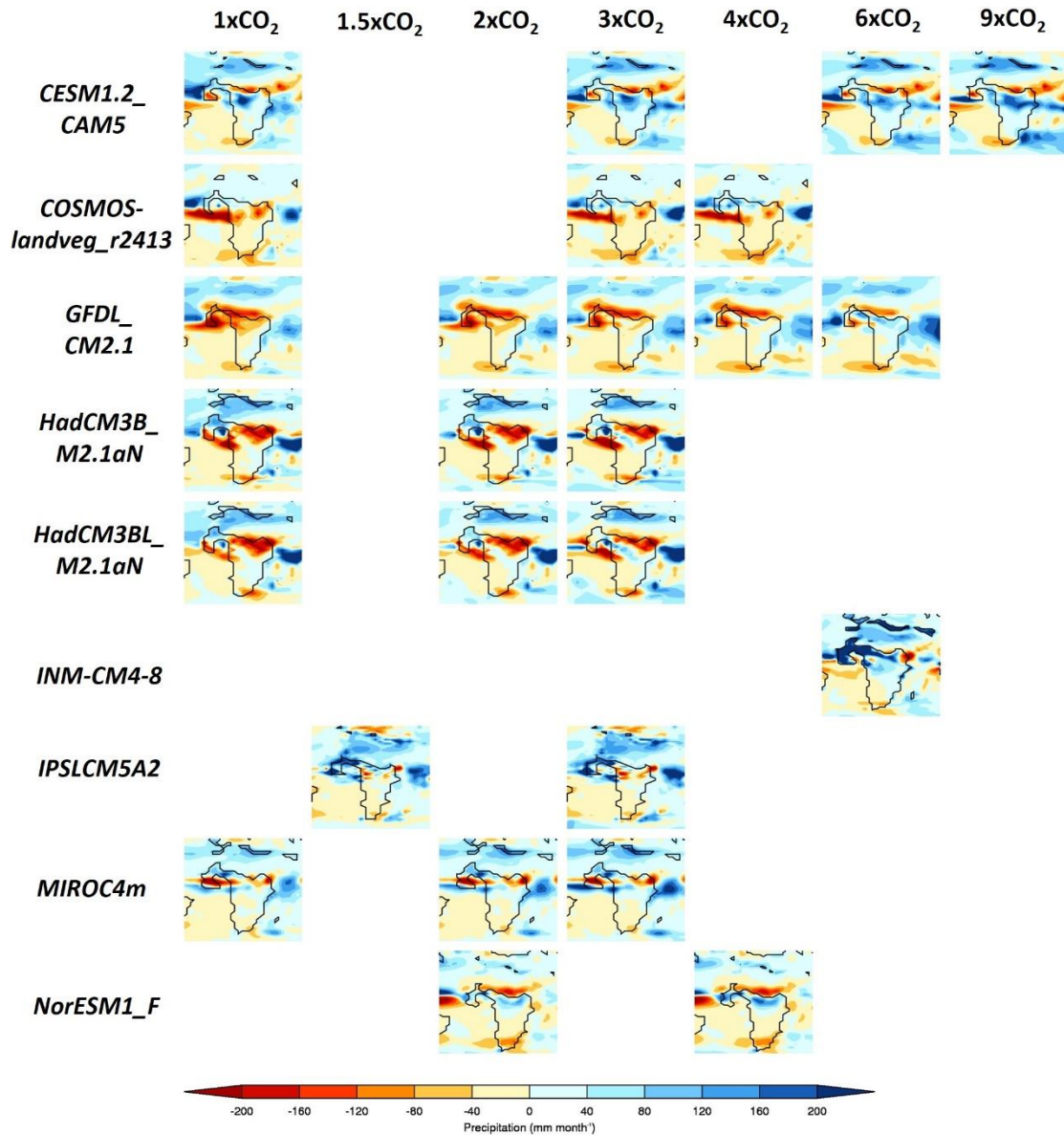


Figure 4 - JJA precipitation climatology differences (early Eocene - PI), for each CO<sub>2</sub> simulation from each model

There is no clear linear trend in either wetting or drying across early Eocene Africa as the CO<sub>2</sub> concentrations increase (Figure 4). Although many models show drying (relative to the PI) of up to ~180 mm month<sup>-1</sup> across northern and western Africa in the 1x, 2x and 3x experiments, this gradually disappears as higher CO<sub>2</sub> concentrations are applied, with some models showing precipitation increases of over 200 mm month<sup>-1</sup> (Figure 4). Some models disagree regardless of experiment, such as GFDL\_CM2.1 which shows drying over northern Africa in all CO<sub>2</sub> experiments contrasting with IPSLCM5A2 which shows wetting over northern Africa in all CO<sub>2</sub> experiments. Further south, none of the models in any of the experiments are showing a large precipitation response. In very general terms, however, at the lower levels of CO<sub>2</sub> concentrations (i.e. up to 4x) the majority of models are showing the same region of drying over northern and western Africa.

### 3.2.2. Lower and higher CO<sub>2</sub> experiments: impact of CO<sub>2</sub>

To investigate the impact of increasing CO<sub>2</sub> on precipitation, when all other boundary conditions are constant, the experiments have been divided into two samples, each containing a different number of models going into the MME: i) “lower-level CO<sub>2</sub>”, namely the 1x, 2x and 3x experiments, comprising four models (GFDL\_CM2.1, HadCM3B\_M2.1aN, HadCM3BL\_M2.1aN and MIROC4m); and ii) “higher-level CO<sub>2</sub>”, namely the 3x and 6x experiments, comprising two models (CESM1.2\_CAM5 and GFDL\_CM2.1); see Table 1. Note that the MMEs for the two 3x experiments are slightly different because they contain a different number of models. Here, both absolute precipitation values and anomalies are shown, where the anomalies are of a certain CO<sub>2</sub> experiment versus another CO<sub>2</sub> experiment, rather than early Eocene versus PI.

The MME absolute precipitation and anomalies for the lower-level sample of CO<sub>2</sub> experiments, are shown in Figure 5a. When the absolute values are considered (Figure 5a, top row), all experiments show regions of precipitation maxima over the equatorial Atlantic (north of the Equator) and West Africa. Over the same West African region as described above (20°W-15°E, 0-20°N, land points only), mean JJA precipitation is 192 mm month<sup>-1</sup>, 201 mm month<sup>-1</sup> and 207 mm month<sup>-1</sup> for the 1x, 2x and 3x experiments, respectively, implying a small increase as CO<sub>2</sub> increases. This becomes more evident when the anomalies are considered (Figure 5a, second row). If the 1x and 2x experiments are compared, the largest change is over the equatorial Atlantic, with a small increase in precipitation of up to 50 mm month<sup>-1</sup> over the Equator and a decrease of over 50 mm month<sup>-1</sup> further north, suggesting a southward displacement of the Atlantic ITCZ. Precipitation is also increased over western Africa. The same pattern is evident when the 1x and 3x experiments are compared, but more pronounced, with both the increases and decreases approaching 100 mm month<sup>-1</sup> in their respective areas.



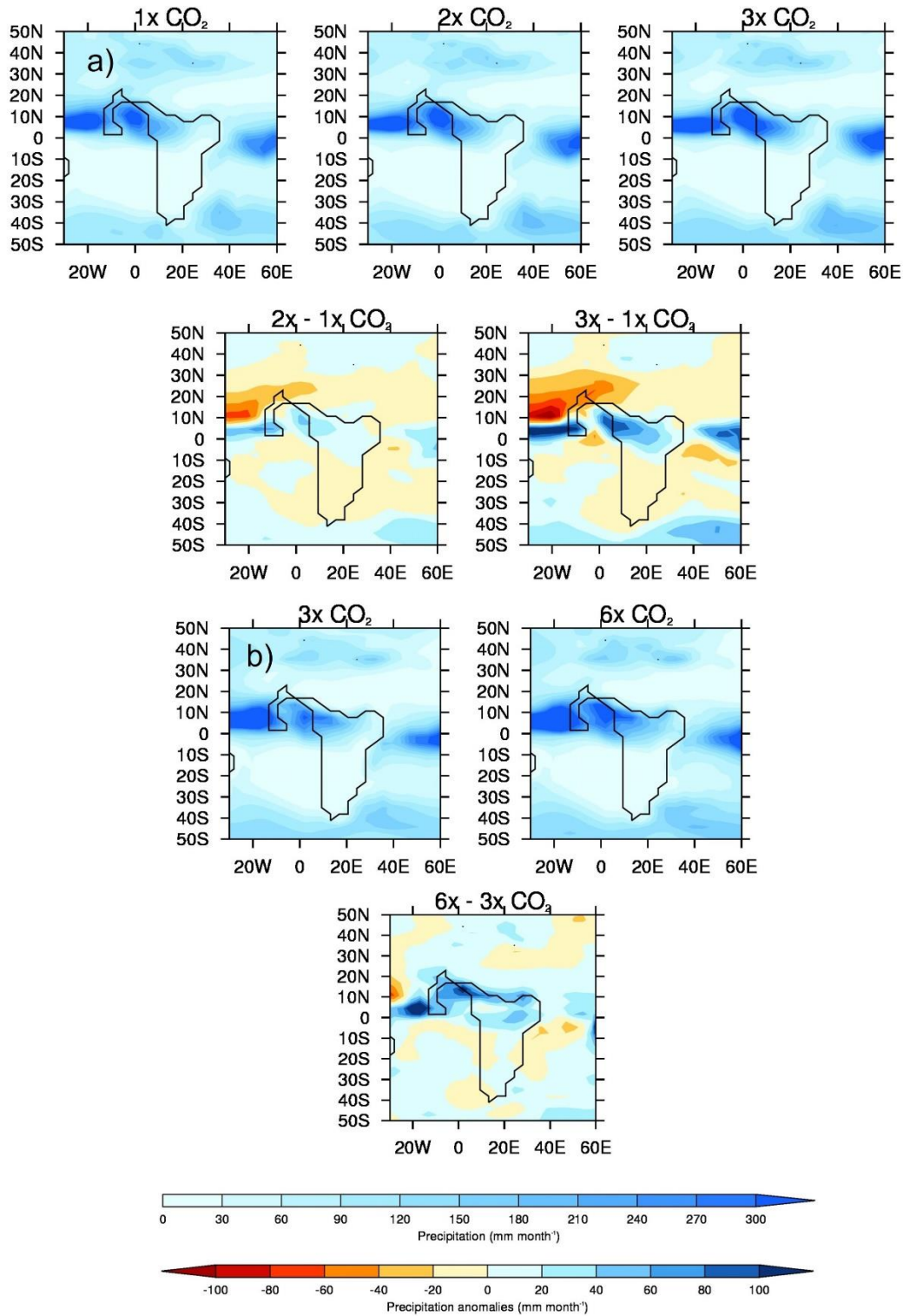


Figure 5 – JJA precipitation multi-model ensemble mean (MME) climatologies and anomalies for the 1x, 2x, 3x and 6x CO<sub>2</sub> experiments, using both samples: a) Lower-level sample of CO<sub>2</sub> experiments (comprising the four models that conducted these: GFDL\_CM2.1, HadCM3B\_M2.1aN, HadCM3BL\_M2.1aN and MIROC4m), absolutes (top row) and anomalies (second row); b) Higher-level sample of CO<sub>2</sub> experiments (comprising the two models that conducted these: CESM1.2\_CAM5 and GFDL\_CM2.1), absolutes (top row) and anomalies (second row)

The MME absolute precipitation and anomalies for the higher-level sample of CO<sub>2</sub> experiments are shown in Figure 5b. When the absolute values are considered (Figure 5b, top row), the region of precipitation maxima in the equatorial Atlantic is larger in the 6x experiment. Over the same West African region, mean JJA precipitation is 186 mm month<sup>-1</sup> and 232 mm month<sup>-1</sup> for the 3x and 6x experiments, respectively, implying a large mean increase as CO<sub>2</sub> increases, and this is further confirmed when the anomalies are considered (Figure 5b, second row). Precipitation increases of over 100 mm month<sup>-1</sup> are shown over the equatorial Atlantic (north of the Equator) and West Africa in the 6x relative to the 3x experiment, but the large region of drying seen at the lower levels of CO<sub>2</sub> is less evident (Figure 5b, second row). This suggests that, whilst West African precipitation is still (and more so here) enhanced as CO<sub>2</sub> rises, it is perhaps less related to Atlantic ITCZ displacement and more related to an increase in south-westerly flow (discussed further in Section 3.3).

### **3.2.3. 1x CO<sub>2</sub> experiment versus preindustrial: impact of non-CO<sub>2</sub> boundary conditions**

The 1x CO<sub>2</sub> experiment versus PI is of particular interest, because this shows the impact of the other boundary conditions rather than that from CO<sub>2</sub> concentrations. When CO<sub>2</sub> concentrations are kept as PI (as in the 1x experiment), the boundary conditions (see Section 2.1) likely to have the largest impact on regional precipitation are the LSM, topography and vegetation (see Figure 1). Although land ice changes, the largest of which during the early Eocene were over the Antarctic Ice Sheet (AIS), do cause a precipitation response (e.g. Kennedy-Asser *et al.* 2019), this is thought to be a mainly local signal and further afield, such as over northern and western Africa during JJA, there is little or no precipitation change when the AIS is either imposed or removed (Kennedy-Asser, pers. comm.).

The MME precipitation anomaly for this experiment is shown in Figure 6a; it should be noted that, although six models conducted this experiment (CESM1.2\_CAM5, COSMOS-landveg\_r2413, GFDL\_CM2.1, HadCM3B\_M2.1aN, HadCM3BL\_M2.1aN and MIROC4m), only the latter four are included here in the MME, to be consistent with the analysis of the CO<sub>2</sub> component (Section 3.2.2). From the available DeepMIP results, it is impossible to disentangle the boundary conditions and ascertain which is dominant in causing the precipitation response; in an ideal world, sensitivity experiments would be conducted to introduce each boundary condition individually, but this is not possible with the results currently available on the DeepMIP database. Nevertheless, based on the results it is possible to theorise which of these boundary conditions might be causing this MME precipitation response. The largest precipitation changes relative to the PI are a small increase in precipitation to the north of early Eocene Africa and in the western Indian Ocean, and a decrease in precipitation over western and northern equatorial Eocene Africa (Figure 6a). It is likely that the northern increases are caused by the change in the LSM (Figure 1a) as this region comprises the preindustrial (and modern) Sahara but is ocean in the early Eocene and therefore would have been a

much greater moisture source. Likewise, the increase over the western Indian Ocean is likely because preindustrial Africa extends much further East than during the early Eocene, again giving much less of a moisture source during the PI (Figure 1a). Moreover, an examination of SST from the early Eocene and PI simulations (from each individual model and the MME) shows that these exposed regions of ocean are characterised by warmer SSTs in the early Eocene; for example, in the Indian Ocean absolute values are up to 32°C in the early Eocene MME compared to up to 28°C in the PI MME, thereby providing a greater source of evaporation during the Eocene see (see Supplementary Material, Figure S3). Concerning the drying over equatorial early Eocene Africa, this is more difficult to interpret and does not seem likely to be related to the LSM or the changes in vegetation. For the LSM, this region of drying coincides with land during both time periods. For the vegetation, although there is a shift in biome between the PI and early Eocene, the region of drying (at approximately 10-20°N) coincides with an increase (or slightly northward shift) in tropical rainforest during the early Eocene, rather than mostly being savanna and grassland in the PI (Figure 1c). This might be expected to result in an increase in precipitation during the early Eocene, rather than a drying. However, this response might be explained by the difference in orographic heights over this region (i.e. over central equatorial Africa), where early Eocene Africa is considerably lower (up to 400 m) than in the PI (up to 1000 m). Finally, over southern Africa, although there is a large increase in orographic heights (of over 1000 m) during the early Eocene (Figure 1b and Figure S1 in the Supplementary Material), this does not appear to be having a large impact on African precipitation, with minimal precipitation differences in the south (Figure 6a).

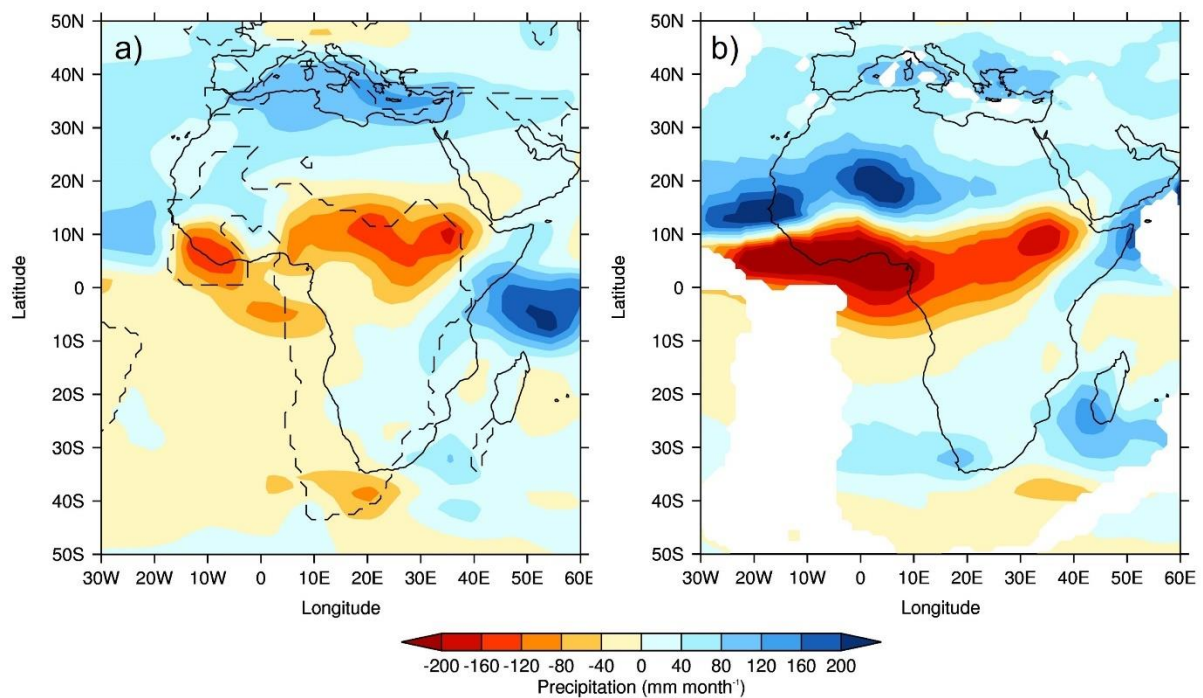


Figure 6 – JJA precipitation multi-model ensemble mean (MME) climatology differences (early Eocene - PI) for the 1x CO<sub>2</sub> experiment (comprising the four models that conducted this experiment, in addition to the others

considered here: GFDL\_CM2.1, HadCM3B\_M2.1aN, HadCM3BL\_M2.1aN and MIROC4m): a) Original (i.e. unrotated) differences; b) Rotated differences i.e. Eocene precipitation rotated forward to where it is in the PI. Note that in a), solid lines show the PI mask and dashed lines show the Eocene mask.

However, a caveat of the above analysis is that, because of the plate rotation differences during the early Eocene, Figure 6a is showing precipitation anomalies that may simply be due to differing geographical locations, rather than any change to the climate state. Therefore, Figure 6b shows the same results, but this time with the early Eocene precipitation rotated forwards (based on the rotations supplied in the Herold *et al.* 2014 Supplementary Material) to where it is in the PI. However, despite these rotational differences, the overall picture remains the same (i.e. increases in precipitation over northern Africa and a decrease in precipitation over western and equatorial Africa) but much more pronounced (Figure 6b). The increases and decreases in precipitation exceed 200 mm month<sup>-1</sup> in some places, suggesting a northward displacement of the Atlantic ITCZ; this difference between the early Eocene and the PI is in contrast to when the Eocene CO<sub>2</sub> experiments are compared with each other, to assess the impact of increasing CO<sub>2</sub> (discussed previously in Section 3.2.2).

### 3.3. Physical mechanisms behind the precipitation response

Here the focus is on the possible dynamic and thermodynamic mechanisms causing the observed precipitation responses, again using the MME absolute values and anomalies from the aforementioned lower-and higher level samples of CO<sub>2</sub> experiments.

The MME absolute 1.5 m surface air temperature (SAT) and anomalies for the lower- and higher-level sample of CO<sub>2</sub> experiments are shown in Figure 7. In line with general understanding there is a clear increase in absolute SAT, everywhere, as the CO<sub>2</sub> increases, with the largest signal (of up to 40°C in the 3x experiment) occurring over the main landmass of central and northern Africa (Figure 7a, top row). This is more obvious when the anomalies are considered, although the largest increases are occurring further south (Figure 7a, second row). This is even more pronounced in the higher-level sample of CO<sub>2</sub> experiments (Figure 7b), and in all experiments the largest increase in SAT, either between the 3x and 1x experiments or the 6x and 3x the experiments, is occurring over southern Africa, away from the largest precipitation changes discussed above. Moreover, the largest increases in precipitation as CO<sub>2</sub> increases (Figure 5) are shown over ocean regions, such as the equatorial Atlantic and off the coast of West early Eocene Africa, whereas the largest increases in SAT (Figure 7) are shown over the landmass. It is likely that these precipitation increases are connected to the warmer SSTs (see Section 3.2.3), or changes to the low-level circulation (discussed below), rather than a direct response to the heating landmass. The Precipitation - Evaporation (P-E) balance (Figure 8) is positive over West Africa in all experiments regardless of sample, corresponding well with the region of increased precipitation (Figure 6), as does cloud cover which is also increasing with CO<sub>2</sub>

over these regions (not shown). Further south, over the Atlantic, the balance is negative implying increased evaporation corresponding to the increased oceanic SAT. Concerning low level circulation, as shown by 850 mb vector winds (Figure 9), when the anomalies are considered (and in particular the 3x versus 1x), there is a small (of up to  $5 \text{ ms}^{-1}$ ) increase in northerly and westerly winds (i.e. clockwise flow) in the equatorial Atlantic north of the Equator (Figure 9a, second row). However, in the higher-level  $\text{CO}_2$  sample (and in particular the anomalies of 6x versus 3x, Figure 9b, second row), this increase in anticyclonic flow is less evident and is instead replaced by a widespread area of increased southwesterly flow across most of the equatorial Atlantic and central Africa. For SAT, P-E and 850 vector winds from each individual model, rather than the MME, see the Supplementary Material (Figure S4a, b, and c, respectively); here, similar to Figure 4, there is no obvious linear change in either P-E or low level circulation as  $\text{CO}_2$  increases, but a clear increase in SAT from all models, in line with current understanding (Figure S4a).

Both the region of enhanced precipitation over West Africa, and the region of drying in the equatorial Atlantic around  $10^\circ\text{N}$ , may be explained by these low-level circulation changes. Up to 3x that of the PI  $\text{CO}_2$ , clockwise low-level circulation increases with  $\text{CO}_2$ , drawing in more moisture from the equatorial Atlantic and causing a relative drying further north, hence the appearance of a southward displacement of the Atlantic ITCZ. At higher levels of  $\text{CO}_2$ , however, where increases in West African precipitation are shown but the region of drying around  $10^\circ\text{N}$  is not, the increased clockwise low-level circulation is replaced by increased south-westerly flow; here, therefore, precipitation is being enhanced by more moisture being drawn in by this south-westerly flow from the warm South Atlantic.

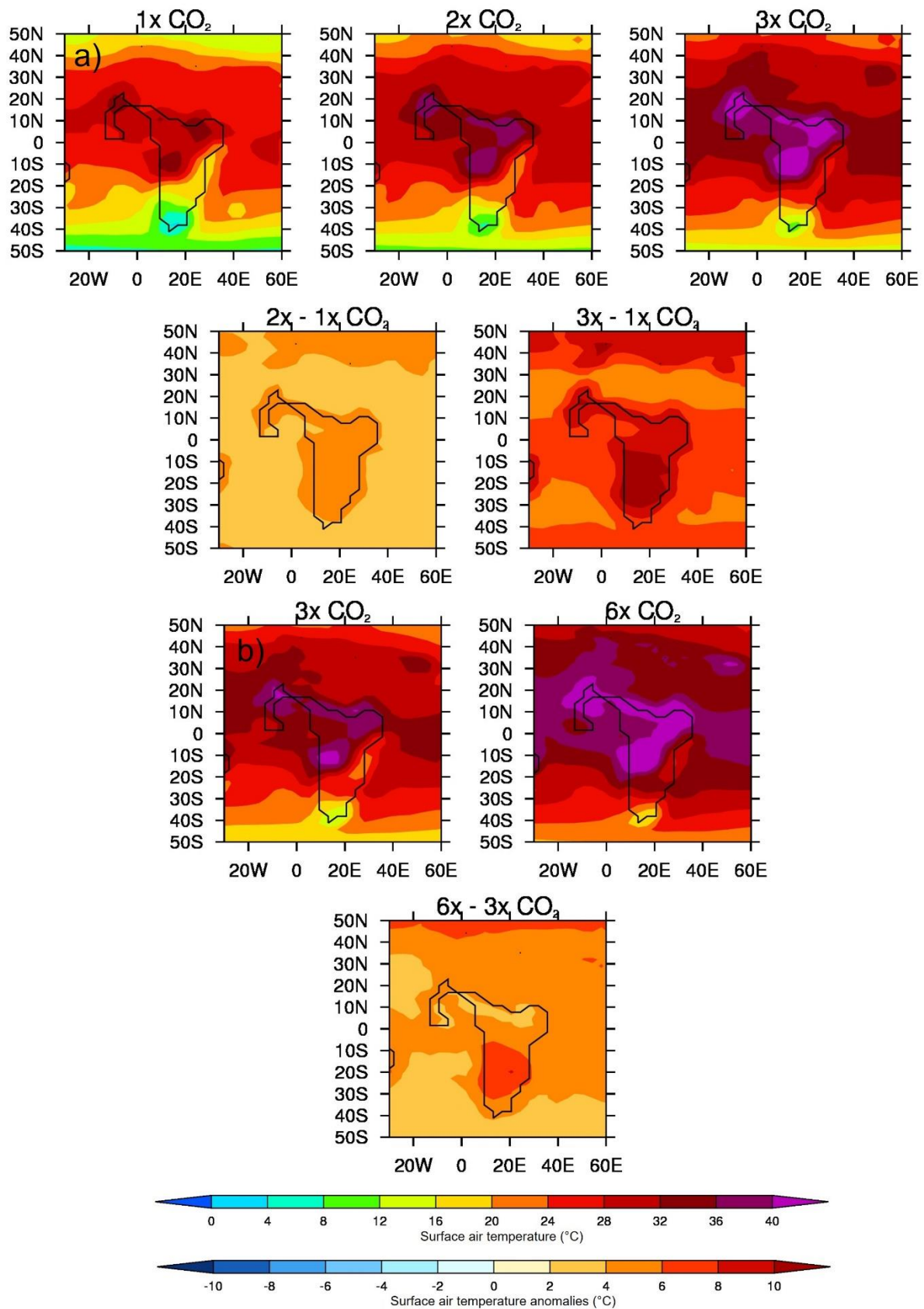


Figure 7 – Same as Figure 5 but for JJA 1.5 m surface air temperature



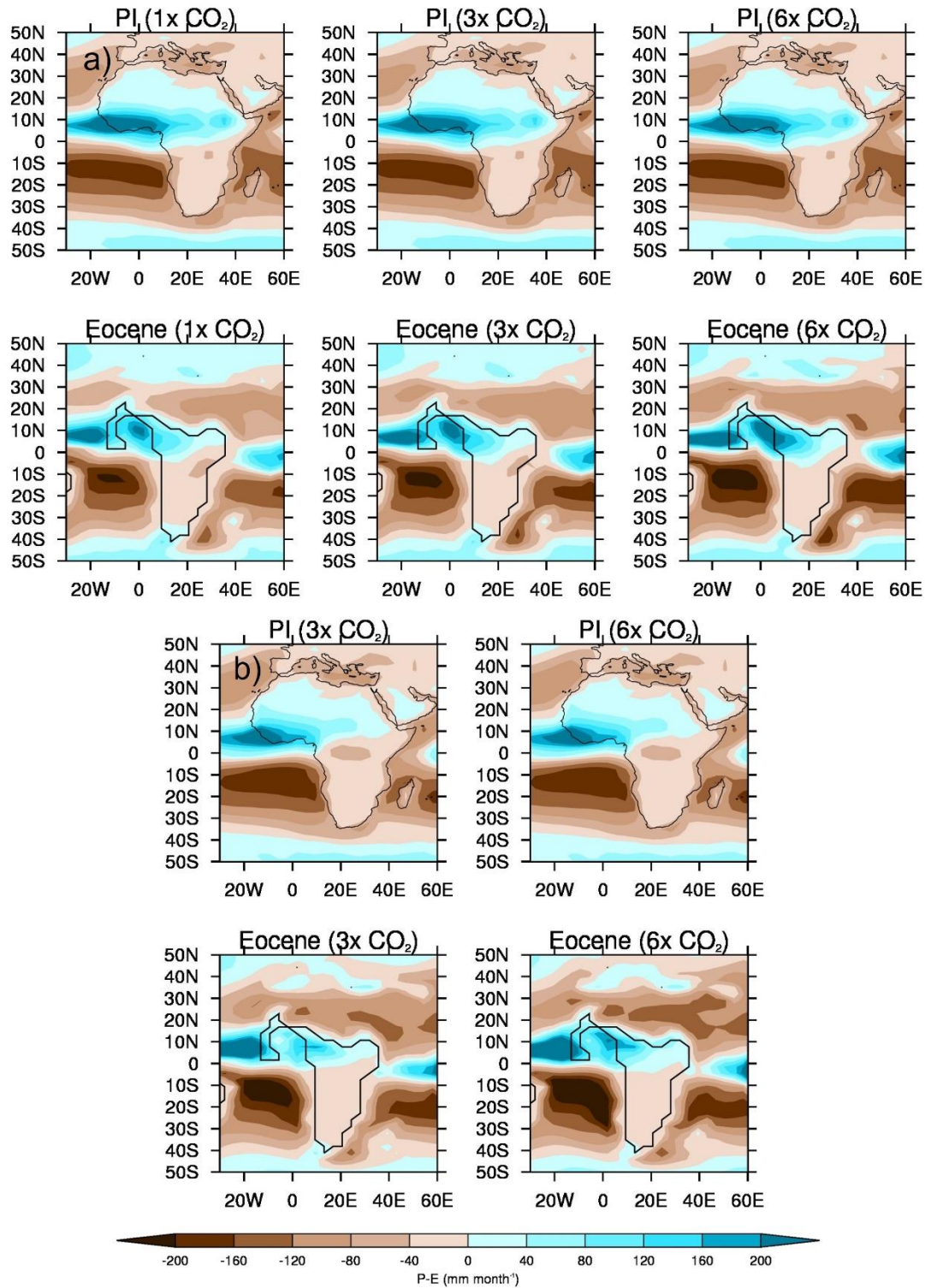
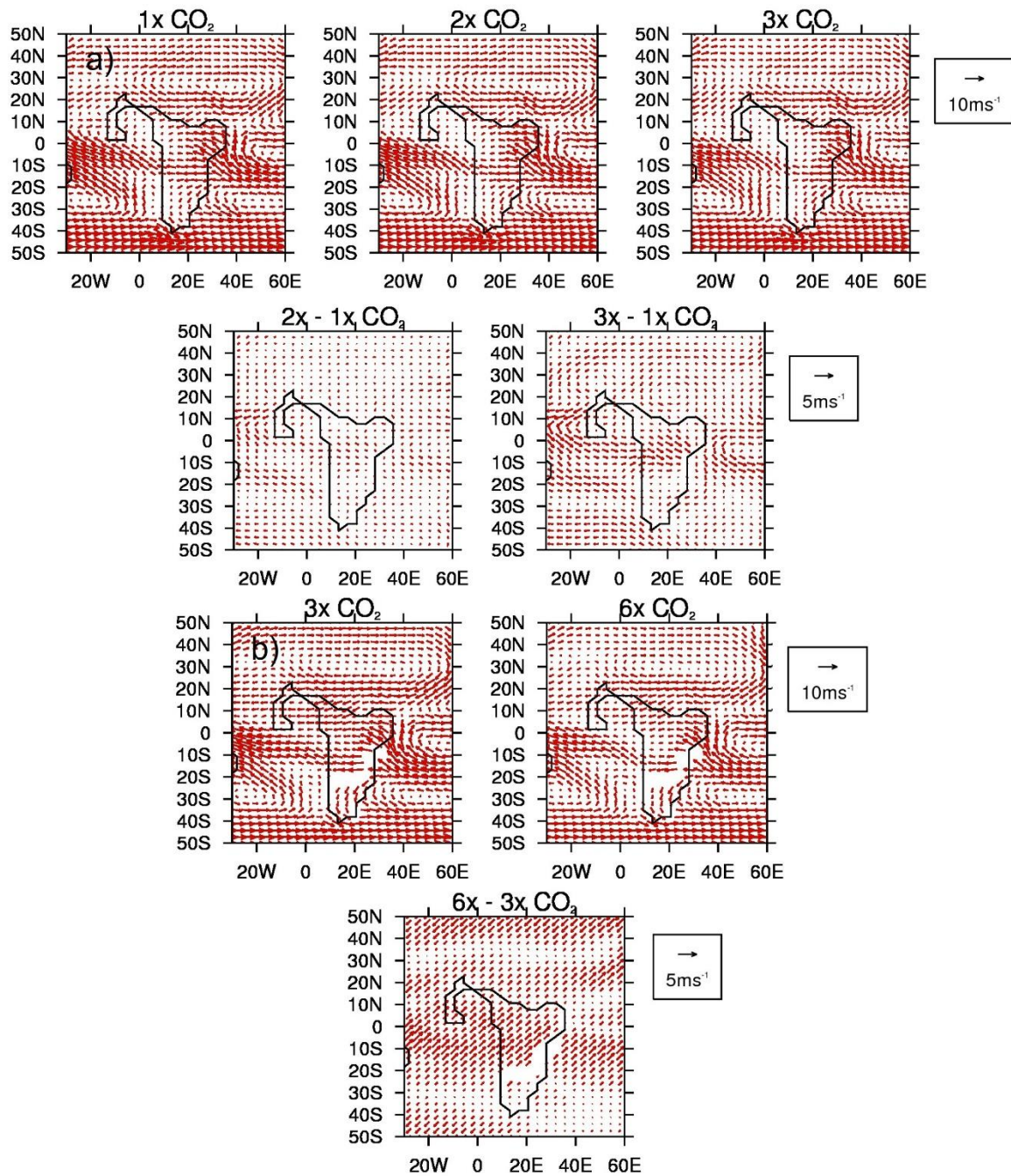


Figure 8 – JJA P-E multi-model ensemble mean (MME) climatology absolutes for the 1x, 2x, 3x and 6x CO<sub>2</sub> experiments, using both samples: a) Lower-level sample of CO<sub>2</sub> experiments (comprising the four models that conducted these: GFDL\_CM2.1, HadCM3B\_M2.1aN, HadCM3BL\_M2.1aN and MIROC4m), PI (top row) and early Eocene (bottom row); b) Higher-level sample of CO<sub>2</sub> experiments (comprising the two models that conducted these: CESM1.2\_CAM5 and GFDL\_CM2.1), PI (top row) and early Eocene (bottom row). Note that the PI panels are identical in each sample because they contain the same models, but are simply replicated here for ease of comparison



751

752 Figure 9 – Same as Figure 5 but for JJA 850 mb wind

753

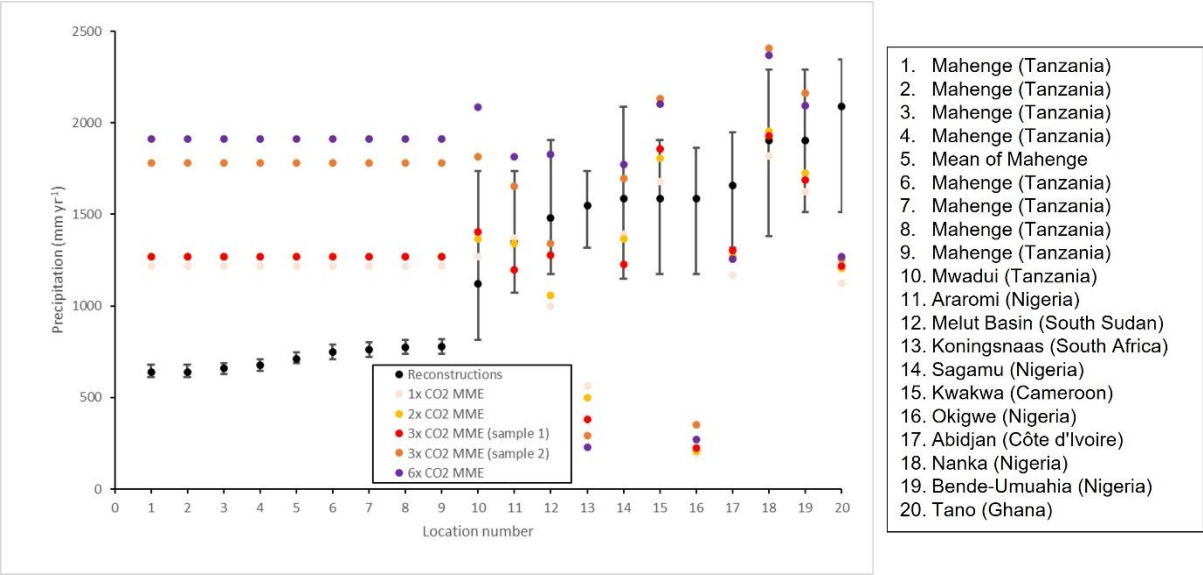
754 **3.4. DeepMIP models' Eocene simulations versus proxy data**

755 In this final section, the focus is on comparing precipitation from selected DeepMIP early Eocene  
756 simulations (using the MME from the same two samples as discussed above) with newly-available  
757 precipitation reconstructions (described in Section 2.3.2). Before the results are presented, however,  
758 several sources of uncertainty in the proxies and models must be noted, aside from analytical  
759 uncertainty that is expressed in the reconstructed confidence intervals. Firstly, the fossil plant  
760 assemblages analysed here have broad age constraints. Palaeofloral assemblages may capture a



snapshot within those age constraints that deviated climatically from the average climatic conditions of a specific age that the model was calibrated on. In addition, fossil plant assemblages tend to preserve better in wetter climates, with drier climates lacking the water bodies needed to preserve plant fossils. Secondly, the DeepMIP models are calibrated on atmospheric CO<sub>2</sub> proxy reconstructions to cover the uncertainty of the entire Eocene; the lower CO<sub>2</sub> levels may be more representative of the late Eocene, but that was not the purpose or interpretation when it came to deciding the experiments. Independent proxies within those ages produce widely variable atmospheric CO<sub>2</sub> reconstructions (e.g. Rae *et al.* 2021), with <500 ppmv from some palaeosol and stomatal reconstructions (Beerling *et al.* 2009; Hyland *et al.* 2013) to >2000 ppmv from boron isotopes and alkenone  $\delta^{13}\text{C}$  (e.g. Bijl *et al.* 2010; Anagnostou *et al.* 2020). It should be noted, however, that there is high uncertainty in these reconstructions; see Hollis *et al.* (2019) for a full discussion. For example, based on a variety of reconstructions compiled as part of the Palaeo-CO<sub>2</sub> project (including phytoplankton, boron proxies, leaf gas exchange, liverworts and nahcolite), atmospheric CO<sub>2</sub> during 55-50 Ma ranges from 500-2000 ppmv (Anagnostou *et al.* 2020, Hollis *et al.* 2019, Westerhold *et al.* 2020). Potentially, these differences in reconstructed atmospheric CO<sub>2</sub> reflect transient climate states (e.g. Reichgelt *et al.* 2016), but regardless, the disagreement between proxy reconstructions makes it problematic to associate a single atmospheric CO<sub>2</sub> level for model-data comparison (Hollis *et al.* 2019). Lastly, a major source of uncertainty is the paucity of proxy data across Africa; as mentioned above, even today there is a lack of long-term climate data over much of Africa, and the same is true for palaeofloras. This sparsity, therefore, is likely responsible for some of the results discussed below, and this is why some of the following results are necessarily partly speculative.

With these caveats in mind, MME MAP at each of the individual locations is shown in Figure 10, ordered according to the reconstructions' values, including uncertainty estimates for the reconstructions (as measured by +/- 1 standard deviation for the locations in Mahenge, Tanzania and the 95% confidence interval for the other 11 locations; see Table 2 for details). The approximate geographical locations can be seen in the Supplementary Material (Figure S5). Firstly it is worth noting that for the majority of reconstructions, uncertainty is high, with a range of up to +/- 1000 mm yr<sup>-1</sup> at some of the locations such as Mwadui, Tanzania (Figure 10). Secondly, whether or not the CO<sub>2</sub> experiments over- or underestimate MAP appears to depend heavily on geographical location, with none of the CO<sub>2</sub> experiments (not even the 6x experiment) reproducing the precipitation amounts of the proxy reconstructions in some locations, such as Koningsnaas, South Africa, Okigwe, Nigeria or Tano, Ghana (Figure 10). Elsewhere, the simulations lie within the uncertainty range of the reconstructions (such as Sagamu or Bende-Umuahia, both in Nigeria), and yet in other places (such as across Kwakwa, Cameroon, and all of the locations at Mahenge, Tanzania) all of the simulations are too wet, by between ~760-1040 mm year<sup>-1</sup> depending on location and CO<sub>2</sub> experiment (Figure 10).



799

800 Figure 10 – Annual mean precipitation from reconstructions (black) and CO<sub>2</sub> experiments multi-model  
801 ensemble mean (MME, colours) at each individual location. Uncertainty in reconstructions is measured by 95%  
802 confidence interval for all sites except Mahenge, where they show +/- 1 standard deviation. Locations have  
803 been ordered according to the reconstructions' values, lowest to highest. Note that locations 1-4 and 6-8 are all  
804 in the same location, but from different stages during the Lutetian (~41-47 Ma), and so have been re-sampled  
805 and averaged into one overall mean (location 5)

806

807 Spatially, MME MAP is shown in Figure 11 (see Figure S6 in the Supplementary Material for each  
808 individual model), showing the uncertainty estimates as concentric circles. As already discussed, the  
809 simulations' precipitation is clearly too high or too low compared to proxy reconstructions in different  
810 parts of Africa. Qualitatively, in very general terms all of the CO<sub>2</sub> experiments are showing wetter  
811 conditions over Western early Eocene Africa (relative to elsewhere), agreeing with Figure 10 where in  
812 many of these locations the models are either within, or at the higher end of, the reconstructions'  
813 uncertainty ranges (Figure 11). Importantly, simulated precipitation over West Africa appears to be  
814 increasing as the CO<sub>2</sub> concentration increases and, in particular for the 6x experiment (Figure 11e), in  
815 this region simulated precipitation exceeds even the upper range of uncertainty of the reconstructions.

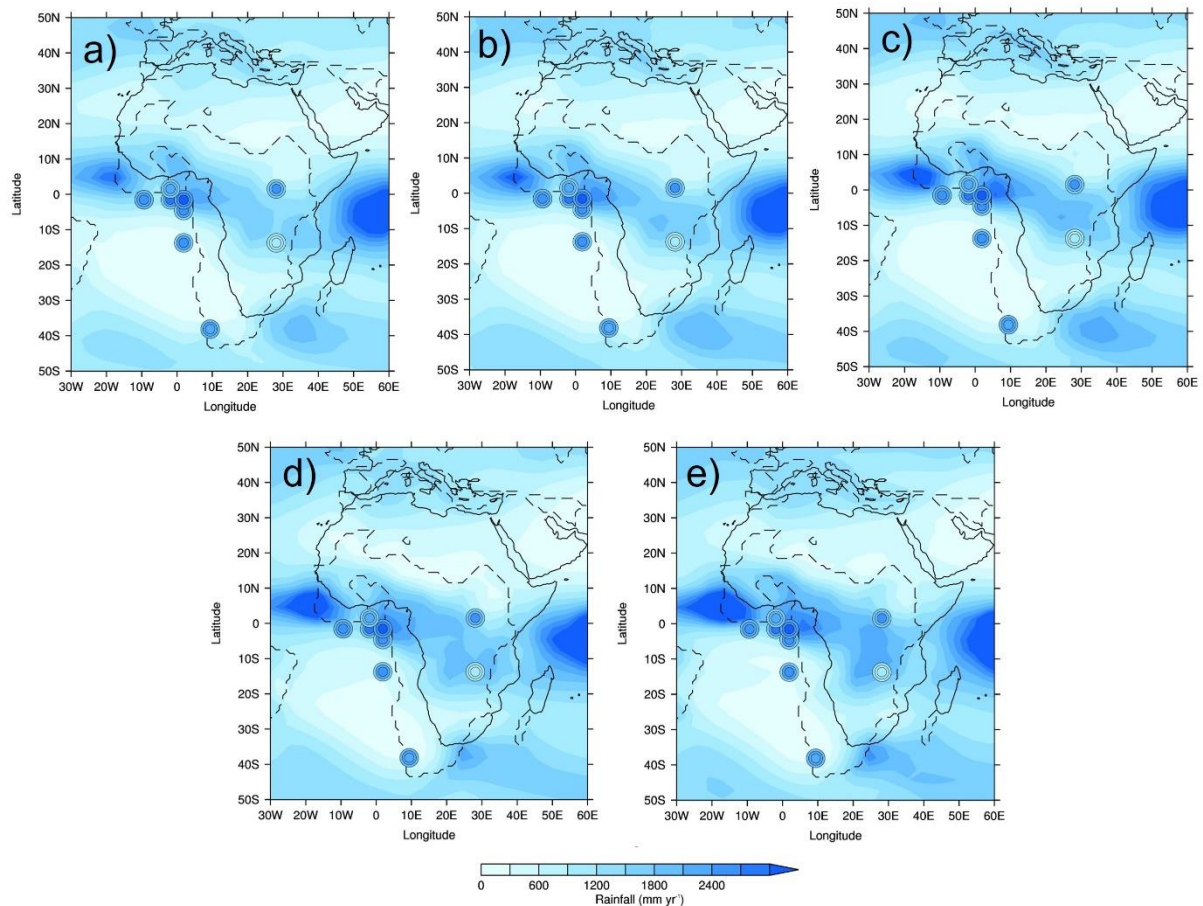


Figure 11 – Annual mean precipitation from reconstructions (circles) and CO<sub>2</sub> experiments multi-model ensemble mean (MME, background gridded data): a) 1x; b) 2x; c) 3x (lower-level CO<sub>2</sub> sample); d) 3x (higher level CO<sub>2</sub> sample); e) 6x. Concentric circles show 95% confidence interval for all sites except Mahenge, where they show +/- 1 standard deviation: outer circle = lower range (or -1 standard deviation), middle circle = average (or, for Mahenge, mode) and inner circle = upper range (or +1 standard deviation). Reconstructions have been rotated forwards to where they are in the PI. Solid lines show the PI mask and dashed lines show the early Eocene mask. Note that, using the common spatial resolution of the MME, 3 reconstructions are all in the same location in West Africa (even though they are in different locations in reality); here, therefore, only the top-most reconstruction is shown

Quantitatively, the root mean squared error (RMSE) between each model (as well as the MME) and the reconstructions at every location is shown in Table 3 and, similar to the anomalies from each model as discussed above, there is no clear relationship between changing CO<sub>2</sub> and a better match to the reconstructions. Most models suggest a better fit to the reconstructions at lower levels of CO<sub>2</sub>, such as CESM1.2\_CAM5 where there is a general increase in RMSE as the CO<sub>2</sub> increases; however, this is not the case for every model, with for example GFDL\_CM2.1 showing a better fit with reconstructions at 2x and 4x CO<sub>2</sub>, rather than higher or lower levels (Table 3). For many of the models and the MME, the 3x CO<sub>2</sub> experiments are showing the least fit with reconstructions. The MME, from the lower-level (but not in the higher-level) CO<sub>2</sub> sample, agrees with this conclusion that

lower CO<sub>2</sub> is giving a slightly better match to the reconstructions, with RMSE values of 758 mm year<sup>-1</sup>, 831 mm year<sup>-1</sup>, 1385 mm year<sup>-1</sup>, 889 mm year<sup>-1</sup> and 839 mm year<sup>-1</sup> for the 1x, 2x, 3x (lower-level CO<sub>2</sub> sample), 3x (higher-level CO<sub>2</sub> sample) and 6x experiments, respectively (Table 3).

	1x CO <sub>2</sub>	1.5x CO <sub>2</sub>	2x CO <sub>2</sub>	3x CO <sub>2</sub>	4x CO <sub>2</sub>	6x CO <sub>2</sub>	9x CO <sub>2</sub>
<b>CESM1.2_CAM5</b>	681			750		704	822
<b>COSMOS-landveg_r2413</b>	699			1424	713		
<b>GFDL_CM2.1</b>	803		762	1027	786	975	
<b>HadCM3B_M2.1aN</b>	796		884	1988			
<b>HadCM3BL_M2.1aN</b>	816		1018	1742			
<b>INM-CM4-8</b>						966	
<b>IPSLCM5A2</b>		744		669			
<b>MIROC4m</b>	614		662	785			
<b>NorESM1_F</b>			1149		1522		
<b>MME (lower-level CO<sub>2</sub> sample)</b>	758		831	1385			
<b>MME (higher-level CO<sub>2</sub> sample)</b>				889		839	

Table 3 - Root Mean Squared Error (RMSE) for mean annual precipitation (MAP) between each model (and multi-model ensemble mean, MME, using both samples) and reconstructions, for each CO<sub>2</sub> experiment

#### 4. DISCUSSION AND CONCLUSIONS

This study has investigated African precipitation during the early Eocene, as simulated by the DeepMIP models. This study is novel, because it investigates the relatively little-studied subject of African hydroclimate during the early Eocene. The results of this study have been divided into four separate sections, corresponding to the four questions posed in Section 1. Firstly, in Section 3.1 the DeepMIP models' PI simulations have been compared to satellite-derived estimates of precipitation, to ascertain how well the models are able to reproduce African precipitation under 'modern' conditions (please see Section 2.3.1 for a discussion of the caveat that here the term 'modern' is actually a combination of both pre-industrial and 20<sup>th</sup>-21<sup>st</sup> century). Secondly, in Section 3.2 the DeepMIP models' early Eocene simulations have been compared to both the PI simulations and each other, to investigate the impact of CO<sub>2</sub> components (i.e. increasing CO<sub>2</sub>) and non-CO<sub>2</sub> components (i.e. other boundary condition changes, such as to the LSM) on African precipitation. Thirdly, in Section 3.3 the CO<sub>2</sub> driven response has been investigated further by looking at a number of dynamic and thermodynamic fields simulated by the models, to ascertain possible physical mechanisms behind the observed precipitation response. Lastly, in Section 3.4 the DeepMIP models' early Eocene simulations have been compared to newly-available proxy data, to indicate how well the models agree with current best precipitation estimates from the Eocene.

The comparison between the DeepMIP PI simulations and modern observations (from TAMSAT) suggest that individual models are both underestimating or overestimating the spatial patterns of African precipitation; this is consistent with Monerie *et al.* (2020), who analysed a number of historical simulations from both CMIP5 and CMIP6 and found that the models' ability to reproduce observations was firstly model dependent and secondly geographically dependent, with many models underestimating precipitation over the Sahel and overestimating it over the Guinea coast and tropical Atlantic. However, here the MME is reducing these biases and is showing the best agreement with TAMSAT in terms of precipitation spatial patterns, highlighting the utility of the MME as a best estimate of the actual precipitation. This has been found elsewhere, such as by Ayugi *et al.* (2021) who looked at East African precipitation in both CMIP5 and CMIP6 models and again found a better performance of the MME relative to individual models, due to systematic errors in individual models being cancelled out. Moreover, Rougier *et al.* (2013) show that it is actually a statistical property of this type of analysis that the ensemble mean will always provide the best match to the data e.g. have the lowest RMSE. It should be noted, however, that a potential caveat of using the MME is that although it eliminates extreme biases, the same models are then being used to run the Eocene simulations, for which the correct (i.e. true) precipitation is less well known and based only on palaeodata, which themselves have uncertainties. Therefore, even using the MME may be propagating its own unknown errors. Concerning the latitudinal extent and seasonal timings of African precipitation, most models show a much wider (latitudinally) West African rain belt compared to TAMSAT and are not reproducing the rapid drop-off in precipitation near the Equator or north of 15°N. This is somewhat in contrast to Monerie *et al.* (2020), who noted that the majority of CMIP5 and CMIP6 models did not have the monsoon extending far enough to the north and were instead showing a southward displacement of precipitation maxima, relative to observations; however, that particular study used the models' historical simulations (as well as a different MME), not pre-industrial as shown here, which may explain the discrepancy. Outside of JJA most models are too wet, but within JJA the results suggest that the drier models (i.e. those underestimating African precipitation) are closer to modern observations than those that are too wet (i.e. overestimating African precipitation).

The comparison between the DeepMIP early Eocene simulations and the PI suggests that, when all individual models are considered separately, there is no obvious wetting or drying trend (relative to the PI) as the CO<sub>2</sub> increases. This is another reason to focus on the MME, which allows easier interpretation as the large model spread is removed. Concerning the non-CO<sub>2</sub> component of precipitation change (i.e. the impact of other boundary conditions when CO<sub>2</sub> is kept at PI levels), the results suggest that changes to the LSM may be responsible for the increases in precipitation (relative to the PI) to the north of early Eocene Africa and the western Indian Ocean, given that these are

‘newly exposed’ regions of ocean in the early Eocene, thereby providing a larger moisture source. In contrast, it is likely that changes in orographic heights are responsible for the region of drying (relative to the PI) over equatorial early Eocene Africa, where early Eocene Africa is considerably lower (up to 400 m) than in the PI (up to 1000 m). When the early Eocene precipitation is rotated forwards in time to where it is in the PI, a similar pattern is shown but is more pronounced, and suggests a northward displacement of the primary rain belt (relative to today), which is consistent with previous work (e.g. Carmichael *et al.* 2016). Concerning the CO<sub>2</sub> component of precipitation change, at the lower levels of increased CO<sub>2</sub> (such as 2x and 3x that of the PI) precipitation over the equatorial Atlantic and West Africa appears to be increasing in response to rising CO<sub>2</sub>, with the concomitant decrease in precipitation north of the equator suggesting a possible displacement of the Atlantic ITCZ towards the south. This therefore suggests that the boundary condition changes imposed for the Eocene are resulting in a northward displacement of the primary rain belt, but increasing CO<sub>2</sub> (with the same boundary conditions) is resulting in a southward displacement of the primary rain belt. At even higher levels of CO<sub>2</sub> (such as 6x that of the PI), precipitation over West Africa is more enhanced relative to the lower levels, but the region of drying is less evident. The enhancement of Northern Hemisphere summer West African precipitation at the highest levels of CO<sub>2</sub> is again consistent with previous work, such as that of Carmichael *et al.* (2016) who showed a generally more intense hydrological cycle at higher CO<sub>2</sub> levels and that of Carmichael *et al.* (2018) who demonstrated an increase in precipitation extremes over tropical Africa at higher CO<sub>2</sub> levels.

Consistent with Carmichael *et al.* (2016), the precipitation increases over West Africa as CO<sub>2</sub> concentrations rise are associated with increased SAT, a strongly positive the P-E balance and cloud cover increases and, concerning temperature, as such are consistent with the idea that a generally warmer world results in a generally wetter world; the ‘wet-gets-wetter and dry-gets-drier’ hypothesis (e.g. Held and Soden 2006). However, the largest increases in SAT shown here are over southern Africa, not where the largest precipitation increases are seen, suggesting factors other than a generally warming world (i.e. dynamical changes) are responsible for the localised precipitation response (see Section 3.3). A caveat to mention here is that, because the DeepMIP simulations use prescribed vegetation rather than interactive, there is no impact on the vegetation types or distribution of these enhanced SATs or precipitation, therefore it is not possible to say whether any enhanced precipitation would be enough to support a certain type of vegetation in the presence of extreme temperatures. Whilst it is likely that the impacts of elevated temperatures and precipitation (whether combined or individually) would be substantial on plant physiology, it is beyond the scope of this study to test this. Sensitivity studies, using interactive vegetation, are currently underway to address these questions.

Lastly, the results from the model-data comparison suggests that whether the early Eocene simulations (regardless of CO<sub>2</sub> experiment) over- or underestimate African precipitation is highly

geographically dependent, with some of the CO<sub>2</sub> experiments at some of the locations lying within the uncertainty range of the reconstructions but others being too wet or too dry. There is some suggestion of a latitudinal relationship, with the simulations overestimating precipitation near the Equator and underestimating precipitation in high latitude regions, such as South Africa; this latter point is consistent with the findings of Carmichael *et al.* (2016). Whether the models are considered independently or whether the MME is used, the results suggest a marginally better fit with the reconstructions at lower levels of CO<sub>2</sub>, and this is in contrast (indirectly) to the findings of Carmichael *et al.* (2016) who suggested the warmest models in the regions of increased precipitation best matched the data; it should be noted, however, that this was a global study. There is no evidence for this here, and indeed the finding of a better match at lower levels of CO<sub>2</sub> is in contrast to that of Reichgelt *et al.* (2022) who focused on Australia and found that the higher, 6x CO<sub>2</sub> experiment was the best match to reconstructions. However, given the uncertainties associated with both the reconstructions (discussed above) and the boundary conditions used to force the models, it is difficult to draw firm conclusions from a model-data comparison of this type. Moreover, a particularly big problem is that, despite the newly-compiled reconstructions presented here, there is still a lack of data across Africa, hindering any firm conclusions. The uncertainties discussed above are likely contributing to the lack of consistency presented in some of these model-data comparisons, such as the MME showing better agreement with the reconstructions at lower and higher levels of CO<sub>2</sub>, but not in between (e.g. the 3x simulation), but this is, at present and given the data sparsity, unavoidable.

In conclusion, therefore, this study has shown that the DeepMIP models are able to approximately reproduce the modern African precipitation and, in response to rising CO<sub>2</sub>, suggest an enhancement of precipitation in this region associated with increasing temperatures and changes to low-level circulation. At very high levels of CO<sub>2</sub> the models may be too wet, relative to proxy reconstructions. However, this might be because the NLR proxy approach has difficulty generating MAP values above modern, or connected to the relatively few early Eocene-aged data points within the reconstructions (meaning some of the comparisons here were necessarily made with data from the middle or late Eocene). Using the MME provides the clearest suggestion of this, but the large amount of model spread means that when individual models are considered, either relative to their corresponding PI simulations or reconstructions, no clear relationship is shown.

## OPEN RESEARCH

TAMSAT data are publicly available to download at <https://www.tamsat.org.uk/>; please see Maidment *et al.* (2014), Maidment *et al.* (2017) and Tarnavsky *et al.* (2014). The palaeobotanical precipitation estimates compiled here are available as a spreadsheet, available to download at Williams (2022). The DeepMIP PI and Eocene simulations are available by following the instructions at <https://www.deepmip.org/data-eocene/>; please see Hollis *et al.* (2019).



## **AUTHOR CONTRIBUTIONS**

CJRW carried out the analysis, produced the figures, wrote the manuscript and led the paper; all authors contributed to writing subsequent drafts of the paper. DJL also carried out some of the analysis, and provided guidance on the scientific discussion. WLC, AAO, YD, DKH, AMB, JBL, PAM, IN, GK, SS, ZZ and JZ carried out the underlying DeepMIP model simulations. US, DRG, GNI and TR collated and synthesised the proxy data. MH and BLOB provided guidance on the scientific discussion and analysis.

## **COMPETING INTERESTS**

The authors declare that they have no conflict of interest.

## **ACKNOWLEDGEMENTS**

CJRW acknowledges the financial support of the UK Natural Environment Research Council funded SWEET project (Super-Warm Early Eocene Temperatures), and that of the European Research Council. WLC and AAO acknowledge funding from JSPS KAKENHI and MEXT KAKENHI, and are grateful to JAMSTEC for use of the Earth Simulator. The numerical simulations performed by DKH and AMB used resources provided by the Swedish National Infrastructure for Computing (SNIC) at the National Supercomputer Centre (NSC), partially funded by the Swedish Research Council. YD and JBL thank GENCI for providing access to the HPC resources of TGCC. PAM thanks Evgeny Volodin and INM RAS for the help with INMCM simulations. GK acknowledges financial support by PACES through the Helmholtz association and the computing centre of the Alfred Wegener Institute in Bremerhaven and the DKRZ in Hamburg (Germany) for computational resources, infrastructure and support. JZ and BLOB acknowledge support from the National Center for Atmospheric Research, which is a major facility sponsored by the National Science Foundation. US acknowledges funding from the Natural Environment Research Council. DRG acknowledges funding from the Natural Sciences and Engineering Council of Canada. GNI acknowledges a GCRF Royal Society Dorothy Hodgkin Fellowship.

## **FINANCIAL SUPPORT**

CJRW was supported by the UK Natural Environment Research Council-funded SWEET project (grant no. NE/P01903X/1) and that of the European Research Council under the European Union's Seventh Framework Programme (FP/2007-868 2013) (ERC grant agreement no. 340923 (TGRES)). WLC and AAO were supported by JSPS KAKENHI (grant no. 17H06104) and MEXT KAKENHI (grant no. 17H06323). AMB and DKH were partially funded by the Swedish Research Council through grant agreement no. 2016-03912 and 2020-04791, and DKH also acknowledges the support of FORMAS grant 2018-01621 and Australian Research Council grant DE220100279. The GFDL



simulations were performed at NSC, partially funded by the Swedish Research Council through grant agreement no. 2018-05973. YD and JBL were supported by GENCI under allocation no. 2019-A0050102212. PAM was supported by the state assignment project no. AAAA-A19-119022190173-2 (FMGE-2019-0009). JZ and BLOB were supported by the National Science Foundation under cooperative agreement no. 1852977. US was supported by the Natural Environment Research Council (grant NE/P019137/1). DRG was supported by the Natural Sciences and Engineering Council of Canada (grant no. 2016-04337). GNI was supported by a GCRF Royal Society Dorothy Hodgkin Fellowship (DHF\R1\191178). MH acknowledges support from NSF OPP 1842059.

## REFERENCES

- Adeonipekun, P. A., Ehinola, O. A., Yussuph, I. A., Toluhi, A. and Oyelami, A.: Bio-sequence stratigraphy of Shagamu Quarry outcrop, Benin Basin, southwestern Nigeria, *World Applied Sciences Journal*, 18, 91-106, DOI: 10.5829/idosi.wasj.2012.18.01.3572, 2012.
- Anagnostou, E., John, E. H., Babila, T. L., Sexton, P. F., Ridgwell, A., Lunt, D. J., Pearson, P. N., Chalk, T. B., Pancost, R. D. and Foster, G. L.: Proxy evidence for state-dependence of climate sensitivity in the Eocene greenhouse, *Nature Communications*, 11(4436), <https://doi.org/10.1038/s41467-020-17887-x>, 2020.
- Anagnostou, E., John, E. H., Edgar, K. M., Foster, G. L., Ridgwell, A., Inglis, G. N., Pancost, R. D., Lunt D. J. and Pearson, P. N.: Changing atmospheric CO<sub>2</sub> concentration was the primary driver of early Cenozoic climate, *Nature*, 533, 380–384, <https://doi.org/10.1038/nature17423>, 2016.
- Arakawa, A. and Schubert, W. H.: Interactions of cumulus cloud ensemble with the large-scale environment. Part I, *J. Atmos. Sci.*, 31, 671-701, [https://doi.org/10.1175/1520-0469\(1974\)031<0674:IOACCE>2.0.CO;2](https://doi.org/10.1175/1520-0469(1974)031<0674:IOACCE>2.0.CO;2), 1974.
- Arias, P. A., Bellouin, N., Coppola, E. et al.: Technical Summary. In *Climate Change 2021: The Physical Science Basis. Contribution of Working Group I to the Sixth Assessment Report of the Intergovernmental Panel on Climate Change* [Masson-Delmotte, V., Zhai, P., Pirani, A., Connors, S. L., Péan, C., Berger, S., Caud, N., Chen, Y., Goldfarb, L., Gomis, M. I., Huang, M., Leitzell, K., Lonnoy, E., Matthews, J. B. R., Maycock, T. K., Waterfield, T., Yelekçi, O., Yu, R. and Zhou, B. (eds.)], Cambridge University Press, In Press, <https://www.ipcc.ch/report/ar6/wg1/#TS>, 2021.
- Atta-Peters, D. and Salami, M. B.: Late Cretaceous to early Tertiary pollen grains from offshore Tano Basin, southwestern Ghana, *Revista Española de Micropaleontología*, 36(3), 451-465, <https://dialnet.unirioja.es/servlet/articulo?codigo=1070295>, 2004.
- Ayugi, B., Zhihong, J., Zhu, H., Ngoma, H., Babaousmail, H., Rizwan, K. and Dike, V.: Comparison of CMIP6 and CMIP5 models in simulating mean and extreme precipitation over East Africa, *Int. J. Clim.*, <https://doi.org/10.1002/joc.7207>, 2021.
- Beerling, D. J., Fox, A. and Anderson, C. W.: Quantitative uncertainty analyses of ancient atmospheric CO<sub>2</sub> estimates from fossil leaves, *AJS*, 309(9), 775-787, DOI: <https://doi.org/10.2475/09.2009.01>, 2009.

Bijl, P. K., Houben, A. J. P., Schouten, S., Bohaty, S. M., Sluijs, A., Reichart, G.-J., Sinninghe  
 Damsté J. S. and Brinkhuis, H.: Transient middle Eocene atmospheric CO<sub>2</sub> and temperature  
 variations, *Science*, 330(6005), 819-821, DOI: 10.1126/science.1193654, 2010.

Bony, S. and Emanuel, K. A.: A parameterization of the cloudiness associated with cumulus  
 convection; evaluation using TOGA COARE data, *J. Atmos. Sci.*, 58(21), 3158-3183,  
[https://doi.org/10.1175/1520-0469\(2001\)058<3158:APOTCA>2.0.CO;2](https://doi.org/10.1175/1520-0469(2001)058<3158:APOTCA>2.0.CO;2), 2001.

Braconnot, P., Harrison, S. P., Otto-Bliesner, B. L., Abe-Ouchi, A., Jungclaus, J. and Peterchmitt, J.-  
 Y.: The palaeoclimate modelling intercomparison project contribution to CMIP5, CLIVAR Exch.  
 Newsl, 56, 15–19, 2011.

Braconnot, P., Otto-Bliesner, B., Harrison, S., Joussaume, S., Peterchmitt, J.-Y., Abe-Ouchi, A.,  
 Crucifix, M., Driesschaert, E., Fichefet, Th., Hewitt, C. D., Kageyama, M., Kitoh, A., Laîné, A.,  
 Loutre, M.-F., Marti, O., Merkel, U., Ramstein, G., Valdes, P., Weber, S. L., Yu, Y., and Zhao, Y.:  
 Results of PMIP2 coupled simulations of the Mid-Holocene and Last Glacial Maximum – Part 1:  
 experiments and large-scale features, *Clim. Past*, 3, 261-277, <https://doi.org/10.5194/cp-3-261-2007>,  
 2007.

Bushell, A. C.: Chapter 2 Understanding the Unified Model (Section 2.1.1), in Matthews, D.: Unified  
 Model User Guide, [http://www.ukscience.org/\\_Media/UM\\_User\\_Guide.pdf](http://www.ukscience.org/_Media/UM_User_Guide.pdf), Accessed 22/9/21, 1998.

Cantrill, D. J., Bamford, M. K., Wagstaff, B. E. and Sauquet, H.: Early Eocene fossil plants from the  
 Mwaui kimberlite pipe, Tanzania, *Review of Palaeobotany and Palynology*, 196, 19-35, DOI:  
 10.1016/j.revpalbo.2013.04.002, 2013.

Carmichael, M. J., Lunt, D. J., Huber, M., Heinemann, M., Kiehl, J., LeGrande, A., Loftson, C. A.,  
 Roberts, C. D., Sagoo, N., Shields, C., Valdes, P. J., Winguth, A., Winguth, C. and Pancost, R. D.: A  
 model-model and data-data comparison for the early Eocene hydrological cycle, *Clim. Past*, 12, 455-  
 481, doi:10.5194/cp-12-455-2016, 2016.

Carmichael, M. J., Pancost, R. D. and Lunt D. J.: Changes in the occurrence of extreme precipitation  
 events at the Paleocene–Eocene thermal maximum, *Earth Planet. Sci. Lett.*, 501, 24-36,  
<https://doi.org/10.1016/j.epsl.2018.08.005>, 2018.

1091 Chan, W.-L., Abe-Ouchi, A. and Ohgaito, R.: Simulating the mid- Pliocene climate with the MIROC  
 1092 general circulation model: experimental design and initial results, *Geosci. Model Dev.*, 4, 1035-1049,  
 1093 <https://doi.org/10.5194/gmd-4-1035-2011>, 2011.  
 1094  
 1095 Chiaghanam, O. I., Chiadikobi, K.C., Oguanya, C.E., Ikegwuonu, O.N., Nwokeabia, C.N.:  
 1096 Palynological and Paleoenvironmental Study of Paleogene in Bende - Umuahia, Niger Delta Basin,  
 1097 Nigeria, *Journal of Environment and Earth Science*, 7, 97-107, ISSN 2225-0948, 2017.  
 1098  
 1099 Cox, P. M.: A primitive equation, 3-dimensional model of the ocean, GFDL Ocean Group Technical  
 1100 Report No. 1, Geophysical Fluid Dynamics Laboratory, Princeton, New Jersey, 1984.  
 1101  
 1102 Cox, P. M., Betts, R. A., Bunton, C. B., Essery, R. L. H., Rowntree, P. R. & Smith, J.: The impact of  
 1103 new land surface physics on the GCM simulation of climate and climate sensitivity. *Clim. Dyn.*,  
 1104 15(3), 183-203. <https://doi.org/10.1007/s003820050276>, 1999.  
 1105  
 1106 Cramwinckel, M. J., Huber, M., Kocken, I. J., Agnini, C., Bijl, P. K., Bohaty, S. M., Frieling, J.,  
 1107 Goldner, A., Hilgen, F. J., Kip, E. L., Peterse, F., van der Ploeg, R., Röhl, U., Schouten, S. and Sluijs,  
 1108 A.: Synchronous tropical and polar temperature evolution in the Eocene, *nature* 559, 382–386,  
 1109 <https://doi.org/10.1038/s41586-018-0272-2>, 2018.  
 1110  
 1111 Crowley, C. W.: An atlas of Cenozoic climates, *Masters of science in geology*, The University of  
 1112 Texas, 2012.  
 1113  
 1114 de Villiers, S. E.: The palynology of Tertiary sediments from a palaeochannel in Namaqualand,  
 1115 Doctor of Philosophy thesis, Faculty of Science, University of Witwatersrand, Johannesburg, 100 pp.,  
 1116 1997.  
 1117  
 1118 Delworth, T. L., Broccoli, A. J., Rosati, A., Stouffer, R. J., Balaji, V., Beesley, J. A., Cooke, W. F.,  
 1119 Dixon, K.W., Dunne, J., Dunne, K. A., Durachta, J. W., Findell, K. L., Ginoux, P., Gnanadesikan, A.,  
 1120 Gordon, C. T., Griffies, S. M., Gudgel, R., Harrison, M. J., Held, I. M., Hemler, R. S., Horowitz, L.  
 1121 W., Klein, S. A., Knutson, T. R., Kushner, P. J., Langenhorst, A. R., Lee, H.-C., Lin, S.-J., Lu, J.,  
 1122 Malyshev, S. L., Milly, P. C. D., Ramaswamy, V., Russell, J., Schwarzkopf, M. D., Shevliakova, E.,  
 1123 Sirutis, J. J., Spelman, M. J., Stern, W. F., Winton, M., Wittenberg, A. T., Wyman, B., Zeng, F. and  
 1124 Zhang, R.: GFDL’s CM2 Global Coupled Climate Models. Part I: Formulation and Simulation  
 1125 Characteristics, *J. Climate*, 19, 643–674, <https://doi.org/10.1175/JCLI3629.1>, 2006.  
 1126

1127 Dufresne, J.-L., Foujols, M.-A., Denvil, S., Caubel, A., Marti, O., Aumont, O., Balkanski, Y., Bekki,  
 1128 S., Bellenger, H., Benshila, R., Bony, S., Bopp, L., Braconnot, P., Brockmann, P., Cadule, P., Cheruy,  
 1129 F., Codron, F., Cozic, A., Cugnet, D., de Noblet, N., Duvel, J.-P., Ethé, C., Fairhead, L., Fichefet, T.,  
 1130 Flavoni, S., Friedlingstein, P., Grandpeix, J.-Y., Guez, L., Guilyardi, E., Hau all glustaine, D.,  
 1131 Hourdin, F., Idelkadi, A., Ghattas, J., Joussaume, S., Kageyama, M., Krinner, G., Labetoulle, S.,  
 1132 Lahellec, A., Lefebvre, M.-P., Lefevre, F., Levy, C., Li, Z. X., Lloyd, J., Lott, F., Madec, G., Mancip,  
 1133 M., Marchand, M., Masson, S., Meurdesoif, Y., Mignot, J., Musat, I., Parouty, S., Polcher, J., Rio, C.,  
 1134 Schulz, M., Swingedouw, D., Szopa, S., Talandier, C., Terray, P., Viovy, N. and Vuichard, N.:  
 1135 Climate Change Projections Using the IPSL-CM5 Earth System Model: From CMIP3 to CMIP5,  
 1136 *Clim. Dynam.*, 40, 2123-2165, <https://doi.org/10.1007/s00382-012-1636-1>, 2013.  
 1137  
 1138 Durre I., Menne, M. J., Gleason, B. E., Houston, T. G. and Vose, R. S.: Comprehensive automated  
 1139 quality assurance of daily surface observations, *J. Applied Meteor. and Climatol.*, 49, 1615-1633,  
 1140 [doi.10.1175/2010JAMC2375.1](https://doi.org/10.1175/2010JAMC2375.1), 2010.  
 1141  
 1142 Durre I., Menne, M. J. and Vose, R. S.: Strategies for evaluating quality assurance procedures, *J.*  
 1143 *Applied Meteor. and Climatol.*, 47, 1785-1791, [doi:10.1175/2007JAMC1706.1](https://doi.org/10.1175/2007JAMC1706.1), 2008.  
 1144  
 1145 Eaton, B.: User's Guide to the Community Atmosphere Model CAM-CAM-5.1.1, NCAR  
 1146 ([https://www.cesm.ucar.edu/models/cesm1.0/cam/docs/ug5\\_1\\_1/ug.html](https://www.cesm.ucar.edu/models/cesm1.0/cam/docs/ug5_1_1/ug.html)), Accessed 10/9/21, 2010.  
 1147  
 1148 Edwards, J. M. and Slingo, A.: Studies with a flexible new radiation code. I: Choosing a configuration  
 1149 for a large-scale model. *Q.J.R. Meteorol. Soc.*, 122: 689-719. <https://doi.org/10.1002/qj.49712253107>,  
 1150 1996.  
 1151  
 1152 Eisawi, A. and Schrank, E.: Upper Cretaceous to Neogene palynology of the Melut Basin, southeast  
 1153 Sudan, *Palynology*, 32, 101-129, DOI: 10.1080/01916122.2008.9989653, 2008.  
 1154  
 1155 Emanuel, K. A.: A scheme for representing cumulus convection in large-scale models, *J. Atmos. Sci.*,  
 1156 48(21), 2313-2329, [https://doi.org/10.1175/1520-0469\(1991\)0482.0.CO;2](https://doi.org/10.1175/1520-0469(1991)0482.0.CO;2), 1991.  
 1157  
 1158 Eyring, V., Bony, S., Meehl, G. A., Senior, C. A., Stevens, B., Stouffer, R. J., and Taylor, K. E.:  
 1159 Overview of the Coupled Model Intercomparison Project Phase 6 (CMIP6) experimental design and  
 1160 organization, *Geosci. Model Dev.*, 9, 1937-1958, [doi:10.5194/gmd-9-1937-2016](https://doi.org/10.5194/gmd-9-1937-2016), 2016.  
 1161  
 1162 Farnsworth, A., Lunt, D. J., Robinson, S.A., Valdes, P.J., Roberts, W.H.G., Clift, P.D., Markwick, P.,  
 1163 Su, T., Wrobel, N., Bragg, F., Kelland, S.J. and Pancost, R.D.: Past East Asian monsoon evolution

controlled by paleogeography, not CO<sub>2</sub>. *Science Advances*, 5, 10, DOI: 10.1126/sciadv.aax1697, 2019.

Fouquart, Y. and Bonnel, B.: Computations of solar heating of the Earth's atmosphere: A new parameterization, *Beitr. Phys. Atmos.*, 53, 35-62, 1980.

Funk, C., Nicholson, S., Landsfeld, M., Klotter, D., Peterson, P. and Harrison, L.: The Centennial Trends Greater Horn of Africa precipitation dataset, *Sci Data* 2, 150050, <https://doi.org/10.1038/sdata.2015.50>, 2015.

Galbraith, E. D., Kwon, E. Y., Gnanadesikan, A., Rodgers, K. B., Griffies, S. M., Bianchi, D., Sarmiento, J. L., Dunne, J. P., Simeon, J., Slater, R. D., Wittenberg, A. T. and Held, I. M.: Climate Variability and Radiocarbon in the CM2Mc Earth System Model, *J. Clim.*, 24, 4230-4254, <https://doi.org/10.1175/2011JCLI3919.1>, 2011.

Gaskell, D. E., Huber, M., O'Brien, C. L., Inglis, G. N., Acosta, R. P., Poulsen, C. J. and Hull, P. M.: The latitudinal temperature gradient and its climate dependence as inferred from foraminiferal  $\delta^{18}\text{O}$  over the past 95 million years, *PNAS*, 119 (11), <https://doi.org/10.1073/pnas.2111332119>, 2022.

Goha, R. B., Zeli, B. D., Konan, R. Y., Tea-Yassi, J., Kouadio, D. K. and Tahi, I.: Stratigraphie palynologique du Maastrichtien supérieur-Eocène supérieur du bassin sédimentaire offshore de Côte d'Ivoire, Afrique de l'ouest, *International Journal of African Studies*, 6, 40-57, 2016.

Grant, A.: Chapter 2 Understanding the Unified Model (Section 2.1.6), in Matthews, D.: *Unified Model User Guide*, [http://www.ukscience.org/\\_Media/UM\\_User\\_Guide.pdf](http://www.ukscience.org/_Media/UM_User_Guide.pdf), Accessed 22/9/21, 1998.

Guo, C., Bentsen, M., Bethke, I., Ilicak, M., Tjiputra, J., Toniazzo, T., Schwinger, J. and Otterå, O. H.: Description and evaluation of NorESM1\_F: a fast version of the Norwegian Earth System Model (NorESM), *Geosci. Model Dev.*, 12, 343-362, <https://doi.org/10.5194/gmd-12-343-2019>, 2019.

Hack, J. J.: Parameterization of moist convection in the NCAR Community Climate Model CCM2, *J. Geophys. Res. Atmos.*, 99(D3): 5551-5568, DOI:10.1029/93JD03478, 1994.

Hagemann, S.: An improved land surface parameter dataset for global and regional climate models, Max Planck Institute for Meteorology, Report No. 336, <https://citeseerx.ist.psu.edu/viewdoc/download?doi=10.1.1.471.2882&rep=rep1&type=pdf>, Accessed 17/9/21, 2002.

1201  
1202 Harrison, S. P. and Prentice, I. C.: Climate and CO<sub>2</sub> controls on global vegetation distribution at the  
1203 last glacial maximum: analysis based on palaeovegetation data, biome modelling and palaeoclimate  
1204 simulations, *Glob. Change Bio.*, 9 (7), 983-1004, <https://doi.org/10.1046/j.1365-2486.2003.00640.x>,  
1205 2003.  
1206  
1207 Harrison, S. P., Bartlein, P. J., Brewer, S., Prentice, I. C., Boyd, M., Hessler, I., Holmgren, K., Izumi,  
1208 K. and Willis, K.: Climate model benchmarking with glacial and mid-Holocene climates, *Clim. Dyn.*,  
1209 43, 671-688, <https://doi.org/10.1007/s00382-013-1922-6>, 2014.  
1210  
1211 Hasumi, H.: CCSR Ocean Component Model (COCO) Version 2.1, Technical Report, The University  
1212 of Tokyo, Tokyo, Japan, 2000.  
1213  
1214 Haywood, A. M., Tindall, J. C., Dowsett, H. J., Dolan, A. M., Foley, K. M., Hunter, S. J., Hill, D. J.,  
1215 Chan, W.-L., Abe-Ouchi, A., Stepanek, C., Lohmann, G., Chandan, D., Peltier, W. R., Tan, N.,  
1216 Contoux, C., Ramstein, G., Li, X., Zhang, Z., Guo, C., Nisancioglu, K. H., Zhang, Q., Li, Q., Kamae,  
1217 Y., Chandler, M. A., Sohl, L. E., Otto-Bliesner, B. L., Feng, R., Brady, E. C., von der Heydt, A. S.,  
1218 Baatsen, M. L. J. and Lunt, D. J.: The Pliocene Model Intercomparison Project Phase 2: large-scale  
1219 climate features and climate sensitivity, *Clim. Past*, 16, 2095-2123, [https://doi.org/10.5194/cp-16-](https://doi.org/10.5194/cp-16-2095-2020)  
1220 2095-2020, 2020.  
1221  
1222 Held, I. M. and Soden, B. J.: Robust Responses of the Hydrological Cycle to Global Warming, *J.*  
1223 *Clim.*, 19 (21), 5686-5699, DOI: <https://doi.org/10.1175/JCLI3990.1>, 2006.  
1224  
1225 Herold, N., Buzan, J., Seton, M., Goldner, A., Green, J. A. M., Müller, R. D., Markwick, P. and  
1226 Huber, M.: A suite of early Eocene (~55 Ma) climate model boundary conditions, *Geosci. Model*  
1227 *Dev.*, 7, 2077-2090, doi:10.5194/gmd-7-2077-2014, 2014.  
1228  
1229 Hijmans, R. J., Cameron, S. E., Parra, J. L., Jones, P. G. and Jarvis, A.: Very high resolution  
1230 interpolated climate surfaces for global land areas, *Int. J. Clim.*, 25, 1965-1978,  
1231 <https://doi.org/10.1002/joc.1278>, 2005.  
1232  
1233 Huber, M. and Caballero, R.: The early Eocene equable climate problem revisited, *Clim. Past*, 7, 603-  
1234 633, doi:10.5194/cp-7-603-2011, 2011.  
1235  
1236 Hurrell, J. W., Holland, M. M., Gent, P. R., Ghan, S., Kay, J. E., Kushner, P. J., Lamarque, J. F.,  
1237 Large, W. G., Lawrence, D., Lindsay, K., Lipscomb, W. H., Long, M. C., Mahowald, N., Marsh, D.

1238 R., Neale, R. B., Rasch, P., Vavrus, S., Vertenstein, M., Bader, D., Collins, W. D., Hack, J. J., Kiehl,  
1239 J. T. and Marshall, S.: The community earth system model: A framework for collaborative research,  
1240 B. Am. Meteorol. Soc., 94, 1339-1360, <https://doi.org/10.1175/BAMS-D-12-00121.1>, 2013.

1241

1242 Hutchinson, D. K., de Boer, A. M., Coxall, H. K., Caballero, R., Nilsson, J. and Baatsen, M.: Climate  
1243 sensitivity and meridional overturning circulation in the late Eocene using GFDL CM2.1, *Clim. Past*,  
1244 14, 789-810, <https://doi.org/10.5194/cp-14-789-2018>, 2018.

1245

1246 Hollis, C. J., Dunkley Jones, T., Anagnostou, E., Bijl, P. K., Cramwinckel, M. J., Cui, Y., Dickens, G.  
1247 R., Edgar, K. M., Eley, Y., Evans, D., Foster, G. L., Frieling, J., Inglis, G. N., Kennedy, E. M.,  
1248 Kozdon, R., Lauretano, V., Lear, C. H., Littler, K., Lourens, L., Meckler, A. N., Naafs, B. D. A.,  
1249 Pälike, H., Pancost, R. D., Pearson, P. N., Röhl, U., Royer, D. L., Salzmann, U., Schubert, B. A.,  
1250 Seebeck, H., Sluijs, A., Speijer, R. P., Stassen, P., Tierney, J., Tripathi, A., Wade, B., Westerhold, T.,  
1251 Witkowski, C., Zachos, J. C., Zhang, Y. G., Huber, H. and Lunt, D. J.: The DeepMIP contribution to  
1252 PMIP4: methodologies for selection, compilation and analysis of latest Paleocene and early Eocene  
1253 climate proxy data, incorporating version 0.1 of the DeepMIP database, *Geosci. Model Dev.*, 12,  
1254 3149–3206, <https://doi.org/10.5194/gmd-12-3149-2019>, 2019.

1255

1256 Holtslag, A. and Boville, B.: Local versus nonlocal boundary-layer diffusion in a global climate  
1257 model, *J. Clim.*, 6, 1825-1825, [https://doi.org/10.1175/1520-0442\(1993\)006<1825:LVNBLD>2.0.CO;2](https://doi.org/10.1175/1520-0442(1993)006<1825:LVNBLD>2.0.CO;2), 1993.

1258

1259

1260 Hyland, E., Sheldon, N. D. and Fan, M.: Terrestrial paleoenvironmental reconstructions indicate  
1261 transient peak warming during the early Eocene climatic optimum, *Geol. Soc. Am. Bull.*, 125(7-8),  
1262 1338-1348, DOI:10.1130/B30761.1, 2013.

1263

1264 Inglis, G. N., Bragg, F., Burls, N. J., Cramwinckel, M. J., Evans, D., Foster, G. L., Huber, M., Lunt,  
1265 D. J., Siler, N., Steinig, S., Tierney, J. E., Wilkinson, R., Anagnostou, E., de Boer, A. M., Dunkley  
1266 Jones, T., Edgar, K. M., Hollis, C. J., Hutchinson, D. K., and Pancost, R. D.: Global mean surface  
1267 temperature and climate sensitivity of the early Eocene Climatic Optimum (EECO), Paleocene–  
1268 Eocene Thermal Maximum (PETM), and latest Paleocene, *Clim. Past*, 16, 1953-1968,  
1269 <https://doi.org/10.5194/cp-16-1953-2020>, 2020.

1270

1271 IPCC: Climate Change 2013: The Physical Science Basis. Contribution of Working Group I to the  
1272 Fifth Assessment Report of the Intergovernmental Panel on Climate Change [Stocker, T. F., D. Qin,  
1273 G.-K. Plattner, M. Tignor, S. K. Allen, J. Boschung, A. Nauels, Y. Xia, V. Bex and P. M. Midgley



1274 (eds.)), Cambridge University Press, Cambridge, United Kingdom and New York, NY, USA, pp  
 1275 1535, <https://www.ipcc.ch/report/ar5/wg1/>, 2013.  
 1276  
 1277 IPCC: Climate Change 2021: The Physical Science Basis. Contribution of Working Group I to the  
 1278 Sixth Assessment Report of the Intergovernmental Panel on Climate Change [Masson-Delmotte, V.,  
 1279 P. Zhai, A. Pirani, S.L. et al. (eds.)], Cambridge University Press, Cambridge, United Kingdom,  
 1280 <https://www.ipcc.ch/report/ar6/wg1/>, 2021.  
 1281  
 1282 Jacobs, B. F. and Herendeen, P. S.: Eocene dry climate and woodland vegetation in tropical Africa  
 1283 reconstructed from fossil leaves from northern Tanzania, *Palaeogeography, Palaeoclimatology,*  
 1284 *Palaeoecology*, 213, 115-123, 10.1016/S0031-0182(04)00368-2, 2004.  
 1285  
 1286 Jungclaus, J. H., Keenlyside, N., Botzet, M., Haak, H., Luo, J.-J., Latif, M., Marotzke, J.,  
 1287 Mikolajewicz, U. and Roeckner, E.: Ocean circulation and tropical variability in the coupled model  
 1288 ECHAM5/MPI-OM, *J. Climate*, 19, 3952-3972, <https://doi.org/10.1175/JCLI3827.1>, 2006.  
 1289  
 1290 K-1 model developers: K-1 coupled model (MIROC) description, Technical Report, Center for  
 1291 Climate System Research (University of Tokyo), National Institute for Environmental Studies,  
 1292 Frontier Research Center for Global Change, Tokyo, Japan, 2004.  
 1293  
 1294 Kageyama, M., Braconnot, P., Harrison, S. P., Haywood, A. M., Jungclaus, J. H., Otto-Bliesner, B. L.,  
 1295 Peterschmitt, J.-Y., Abe-Ouchi, A., Albani, S., Bartlein, P. J., Brierley, C., Crucifix, M., Dolan, A.,  
 1296 Fernandez-Donado, L., Fischer, H., Hopcroft, P. O., Ivanovic, R. F., Lambert, F., Lunt, D. J.,  
 1297 Mahowald, N. M., Peltier, W. R., Phipps, S. J., Roche, D. M., Schmidt, G. A., Tarasov, L., Valdes, P.  
 1298 J., Zhang, Q. and Zhou, T.: The PMIP4 contribution to CMIP6 – Part 1: Overview and over-arching  
 1299 analysis plan, *Geosci. Model Dev.*, 11, 1033–1057, <https://doi.org/10.5194/gmd-11-1033-2018>, 2018.  
 1300  
 1301 Kaiser, T. M. Ansorge, J., Arratia, G., Bullwinkel, V., Gunnell, G. F., Herendeen, P. S., Jacobs, B.,  
 1302 Mingram, J., Msuya, C., Musolff, A., Naumann, R., Schulz, E. and Wilde, V.: The maar lake of  
 1303 Mahenge (Tanzania) unique evidence of Eocene terrestrial environments in sub-Saharan Africa,  
 1304 *Zeitschrift der Deutschen Gesellschaft für Geowissenschaften Band 157 Heft 3*, DOI: 10.1127/1860-  
 1305 1804/2006/0157-0411, 2006.  
 1306  
 1307 Kaplan, J. O., Bigelow, N. H., Prentice, I. C., Harrison, S. P., Bartlein, P. J., Christensen, T. R.,  
 1308 Cramer, W., Matveyeva, N. V., McGuire, A. D., Murray, D. F., Razzhivin, V. Y., Smith, B., Walker,  
 1309 D. A., Anderson, P. M., Andreev, A. A., Brubaker, L. B., Edwards, M. E. and Lozhkin, A. V.:

Climate change and Arctic ecosystems: 2. Modeling, paleodata-model comparisons, and future projections, *J. Geophys. Res.*, 108, 8171, doi:10.1029/2002jd002559, 2003.

Keery, J. S., Holden, P. B. and Edwards, N. R.: Sensitivity of the Eocene climate to CO<sub>2</sub> and orbital variability, *Clim. Past*, 14, 215-238, DOI: 10.5194/cp-14-215-2018, 2018

Kennedy-Asser, A. T., Lunt, D. J., Farnsworth, A. and Valdes, P. J.: Assessing mechanisms and uncertainty in modeled climatic change at the Eocene-Oligocene transition, *Paleoceanography and Paleoclimatology*, 34, 16-34. <https://doi.org/10.1029/2018PA003380>, 2019.

Laval, K., Sadourny, R. and Serafini, Y.: Land surface processes in a simplified general circulation model, *Geophys. Astrophys. Fluid Dyn.*, 17(1), 129-150, <https://doi.org/10.1080/03091928108243677>, 1981.

Li, X., Guo, C., Zhang, Z., Otterå, O. H. and Zhang, R.: PlioMIP2 simulations with NorESM-L and NorESM1-F, *Clim. Past*, 16, 183-197, <https://doi.org/10.5194/cp-16-183-2020>, 2020.

Licht, A., van Cappelle, M., Abels, H. Ladant, J.-B., Trabucho-Alexandre, J., France-Lanord, C., Donnadieu, Y., Vandenberghe, J., Rigaudier, T., Lécuyer, C., Terry Jr, D., Adriaens, R., Boura, A., Guo, Z., Naing Soe, A., Quade, J., Dupont-Nivet, G. and Jaeger, J.-J.: Asian monsoons in a late Eocene greenhouse world, *Nature*, 513, 501–506, <https://doi.org/10.1038/nature13704>, 2014.

Liebmann, B., Bladé, I., Kiladis, G. N., Carvalho, L. M. V., Senay, G. B., Allured, D., Leroux, S. and Funk, C.: Seasonality of African Precipitation from 1996 to 2009, *J. Clim.*, 25 (12), 4304-4322, DOI: <https://doi.org/10.1175/JCLI-D-11-00157.1>, 2012.

Liu, W., Xie, S.-P., Liu, Z. and Zhu, J.: Overlooked possibility of a collapsed Atlantic Meridional Overturning Circulation in warming climate, *Science Advances*, 3(1), e1601666. <https://doi.org/10.1126/sciadv.1601666>, 2017.

Liu, X. D., Dong, B. W., Yin, Z. Y., Smith, R. S. and Guo, Q. C.: Continental drift, plateau uplift, and the evolutions of monsoon and arid regions in Asia, Africa, and Australia during the Cenozoic, *Science China-Earth Sciences*, 62, 1053-1075, DOI: 10.1007/s11430-018-9337-8, 2019.

Loftson, C. A., Lunt, D. J. And Francis, J. E.: Investigating vegetation-climate feedbacks during the early Eocene, *Clim. Past*, 10, 419-436, doi:10.5194/cp-10-419-2014, 2014.

1347 Lott, F.: Alleviation of stationary biases in a GCM through a mountain drag parameterization scheme  
 1348 and a simple representation of mountain lift forces, *Mon. Wea. Rev.*, 127(5), 788-801,  
 1349 [https://doi.org/10.1175/1520-0493\(1999\)127<0788:AOSBIA>2.0.CO;2](https://doi.org/10.1175/1520-0493(1999)127<0788:AOSBIA>2.0.CO;2), 1999.  
 1350  
 1351 Louis, J. F.: A parametric model of vertical eddy fluxes in the atmosphere, *Boundary-Layer*  
 1352 *Meteorol.*, 17(2), 187-202, <https://doi.org/10.1007/BF00117978>, 1979.  
 1353  
 1354 Lunt, D. J., Bragg, F., Chan, W.-L., Hutchinson, D. K., Ladant, J.-B., Morozova, P., Niezgodzki, I.,  
 1355 Steinig, S., Zhang, Z., Zhu, J., Abe-Ouchi, A., Anagnostou, E., de Boer, A. M., Coxall, H. K.,  
 1356 Donnadieu, Y., Foster, G., Inglis, G. N., Knorr, G., Langebroek, P. M., Lear, C. H., Lohmann, G.,  
 1357 Poulsen, C. J., Sepulchre, P., Tierney, J. E., Valdes, P. J., Volodin, E. M., Dunkley Jones, T., Hollis,  
 1358 C. J., Huber, M. and Otto-Bliesner, B. L.: DeepMIP: model intercomparison of early Eocene climatic  
 1359 optimum (EECO) large-scale climate features and comparison with proxy data, *Clim. Past*, 17, 203-  
 1360 227, <https://doi.org/10.5194/cp-17-203-2021>, 2021.  
 1361  
 1362 Lunt, D. J., Dunkley Jones, T., Heinemann, M., Huber, M., LeGrande, A., Winguth, A., Loptson, C.,  
 1363 Marotzke, J., Roberts, C. D., Tindall, J., Valdes, P. and Winguth, C.: A model-data comparison for a  
 1364 multi-model ensemble of early Eocene atmosphere-ocean simulations: EoMIP, *Clim. Past*, 8, 1717-  
 1365 1736, <https://doi.org/10.5194/cp-8-1717-2012>, 2012.  
 1366  
 1367 Lunt, D. J., Huber, M., Anagnostou, E., Baatsen, M. L. J., Caballero, R., DeConto, R., Dijkstra, H. A.,  
 1368 Donnadieu, Y., Evans, D., Feng, R., Foster, G. L., Gasson, E., von der Heydt, A. S., Hollis, C. J.,  
 1369 Inglis, G. N., Jones, S. M., Kiehl, J., Kirtland Turner, S., Korty, R. L., Kozdon, R., Krishnan, S.,  
 1370 Ladant, J.-B., Langebroek, P., Lear, C. H., LeGrande, A. N., Littler, K., Markwick, P., Otto-Bliesner,  
 1371 B., Pearson, P., Poulsen, C. J., Salzmann, U., Shields, C., Snell, K., Stärz, M., Super, J., Tabor, C.,  
 1372 Tierney, J. E., Tourte, G. J. L., Tripathi, A., Upchurch, G. R., Wade, B. S., Wing, S. L., Winguth, A.  
 1373 M. E., Wright, N. M., Zachos, J. C. and Zeebe, R. E.: The DeepMIP contribution to PMIP4:  
 1374 experimental design for model simulations of the EECO, PETM, and pre-PETM (version 1.0),  
 1375 *Geosci. Model Dev.*, 10, 889-901, <https://doi.org/10.5194/gmd-10-889-2017>, 2017.  
 1376  
 1377 Ma, Y. Q., Fan, M. J., Lu, Y. C., Liu, H. M., Zhang, S. P. and Liu, X. F.: Stable isotope record of  
 1378 middle Eocene summer monsoon and its instability in eastern China, *Global and Planetary Change*,  
 1379 175, 103-112, DOI: 10.1016/j.gloplacha.2019.02.007, 2019.  
 1380  
 1381 Maidment, R. I., Grimes, D., Black, E., Tarnavsky, E., Young, M., Greatrex, H., Allan, R. P., Stein,  
 1382 T., Nkonde, E., Senkunda, S. and Alcántara, E. M. U.: A new, long-term daily satellite-based rainfall

dataset for operational monitoring in Africa, *nature Scientific Data*, 4: 170063. DOI: 10.1038/sdata.2017.63, 2017.

Maidment, R. I., Grimes, D., Allan, R. P., Tarnavsky, E., Stringer, M., Hewison, T., Roebeling, R. and Black, E.: The 30-year TAMSAT African Rainfall Climatology and Time-series (TARCAT) Data Set, *J. Geophys. Res.: Atmos.*, 119(10): 619-610, 644. DOI: 10.1002/2014JD021927, 2014.

Marsland, S. J., Haak, H., Jungclaus, J. H., Latif, M. and Roske, F.: The Max-Planck-Institute global ocean/sea ice model with orthogonal curvilinear coordinates, *Ocean Model.*, 5, 91-127, [https://doi.org/10.1016/S1463-5003\(02\)00015-X](https://doi.org/10.1016/S1463-5003(02)00015-X), 2003.

Martínez-Botí, M. A., Foster, G. L., Chalk, T. B., Rohling, E. J., Sexton, P. F., Lunt, D. J., Pancost, R. D., Badger, M. P. S. and Schmidt, D. N.: Plio-Pleistocene climate sensitivity evaluated using high-resolution CO<sub>2</sub> records, *Nature*, 518, 49-54, <https://doi.org/10.1038/nature14145>, 2015.

Menne, M. J., Durre I., Vose, R. S., Gleason, B. E. and Houston, T. G.: An overview of the Global Historical Climatology Network-Daily Database, *J. Atmos. and Oceanic Tech.*, 29, 897-910, doi.10.1175/JTECH-D-11-00103.1, 2012.

Monerie, P-A., Wainwright, C. M. and Sidibe, M.: Model uncertainties in climate change impacts on Sahel precipitation in ensembles of CMIP5 and CMIP6 simulations, *Clim. Dyn.*, 55, 1385-1401, <https://doi.org/10.1007/s00382-020-05332-0>, 2020.

Moorthi, S. and Suarez, M. J.: Relaxed Arakawa-Schubert. A Parameterization of Moist Convection for General Circulation Models, *Mon. Weather Rev.*, 120, 978-1002, [https://doi.org/10.1175/1520-0493\(1992\)120<0978:RASAPO>2.0.CO;2](https://doi.org/10.1175/1520-0493(1992)120<0978:RASAPO>2.0.CO;2), 1992.

Morcrette, J. J., Smith, L. and Fouquart, Y.: Pressure and temperature dependence of the absorption in longwave radiation parameterizations, *Beitr. Phys. Atmos.*, 59, 455-469, ISSN 0005-8173, 1986.

Morley, R. J.: Cretaceous and Tertiary climate change and the past distribution of megathermal rainforests, in: *Tropical Rainforest Responses to Climatic Change*, Springer Praxis Books, Springer Berlin Heidelberg, 1–31, 2007.

Morrison, H. and Gettelman, A.: A New Two-Moment Bulk Stratiform Cloud Microphysics Scheme in the Community Atmosphere Model, Version 3 (CAM3). Part I: Description and Numerical Tests, *J. Clim.*, 21(15), 3642-3659, DOI:10.1175/2008JCLI2105.1, 2008.

1420

1421 Naafs, B. D. A., Rohrssen, M., Inglis, G. N., Lähteenoja, O., Feakins, S. J., Collinson, M. E.,  
 1422 Kennedy, E. M., Singh, P. K., Singh, M. P., Lunt, D. J. and Pancost, R. D.: High temperatures in the  
 1423 terrestrial mid-latitudes during the early Palaeogene, *Nature Geosci* 11, 766-771,  
 1424 <https://doi.org/10.1038/s41561-018-0199-0>, 2018.

1425

1426 Neale, R. B., Richter, J. H. and Jochum M.: The impact of convection on ENSO: From a delayed  
 1427 oscillator to a series of events, *J. Clim.*, 21(22), 5904-5924, <https://doi.org/10.1175/2008JCLI2244.1>,  
 1428 2008.

1429

1430 Neale, R. B., Richter, J. H., Park, S., Lauritzen, P. H., Vavrus, S. J., Rasch, P. J. and Zhang, M.: The  
 1431 Mean Climate of the Community Atmosphere Model (CAM4) in Forced SST and Fully Coupled  
 1432 Experiments, *J. Clim.*, 26(14), 5150-5168, <https://doi.org/10.1175/JCLI-D-12-00236.1>, 2013.

1433

1434 Okeke, K. K. and Umeji, O. P.: Palynostratigraphy, palynofacies and palaeoenvironment of deposition  
 1435 of Selandian to Aquitanian sediments, southeastern Nigeria, *Journal of African Earth Sciences*, 120,  
 1436 102-124, DOI: 10.1016/j.jafrearsci.2016.04.020, 2016

1437

1438 Park, S. and Bretherton, C. S.: The University of Washington Shallow Convection and Moist  
 1439 Turbulence Schemes and Their Impact on Climate Simulations with the Community Atmosphere  
 1440 Model, *J. Clim.*, 22(12), 3449-3469, DOI:10.1175/2008JCLI2557.1, 2009.

1441

1442 Pearson, P. N. and Wade, B. S.: Stable warm tropical climate through the Eocene Epoch, *Geology*, 35  
 1443 (1), <https://doi.org/10.1130/G24462Y.1>, 2007.

1444

1445 Quan, C., Liu, Y. S. and Utescher, T.: Eocene monsoon prevalence over China: A paleobotanical  
 1446 perspective, *Palaeogeography Palaeoclimatology Palaeoecology*, 365, 302-311, DOI:  
 1447 10.1016/j.palaeo.2012.09.035, 2012.

1448

1449 Rae, J. W. B., Zhang, Y. G., Liu, X., Foster, G. L., Stoll, H. M. and Whiteford, R. D. M.: Atmospheric  
 1450 CO<sub>2</sub> over the past 66 million years from marine archives, *Annual Review of Earth and Planetary*  
 1451 *Sciences*, 49, 606-641, <https://doi.org/10.1146/annurev-earth-082420-063026>, 2021.

1452

1453 Rasch, P. J. and Kristjánsson, J. E.: A comparison of the CCM3 model climate using diagnosed and  
 1454 predicted condensate parameterizations, *J. Clim.*, 11(7), 1587-1614, [https://doi.org/10.1175/1520-0442\(1998\)011<1587:ACOTCM>2.0.CO;2](https://doi.org/10.1175/1520-0442(1998)011<1587:ACOTCM>2.0.CO;2), 1998.

1455

1456

1457 Reichgelt, T., D'Andrea, W. J. and Fox, B. R. S.: Abrupt plant physiological changes in southern New  
 1458 Zealand at the termination of the Mi-1 event reflect shifts in hydroclimate and pCO<sub>2</sub>, *EPSL*, 455, 115–  
 1459 124, <https://doi.org/10.1016/j.epsl.2016.09.026>, 2016.

1460

1461 Reichgelt, T., Greenwood, D. R., Steinig, S., Conran, J. G., Hutchinson, D. K., Lunt, D. J., Scriven, L.  
 1462 J., and Zhu, J.: Plant proxy evidence for high rainfall and productivity in the Eocene of Australia,  
 1463 *Paleoceanography and Paleoclimatology*, <https://doi.org/10.1029/2022PA004418>, 2022.

1464

1465 Richter, J. H. and Rasch, P. J.: Effects of convective momentum transport on the atmospheric  
 1466 circulation in the Community Atmosphere Model, version 3, *J. Clim.*, 21, 1487-1499,  
 1467 <https://doi.org/10.1175/2007JCLI1789.1>, 2008.

1468

1469 Roeckner, E., Bäuml, G., Bonaventura, L., Brokopf, R., Esch, M., Giorgetta, M., Hagemann, S.,  
 1470 Kirchner, I., Kornbleuh, L., Manzini, E., Rhodin, A., Schlese, U., Schulzweida, U. and Tompkins, A.:  
 1471 The atmospheric general circulation model ECHAM 5. PART I: Model description, Report 349, Max-  
 1472 Planck Institut für Meteorologie, Hamburg, Germany, 140 pp., 2003.

1473

1474 Rotstajn, L. D.: A physically based scheme for the treatment of stratiform clouds and precipitation in  
 1475 large-scale models. I: Description and evaluation of the microphysical processes, *Q. J. R. Meteorol.*  
 1476 *Soc.*, 123, 1227–1282, <https://doi.org/https://doi.org/10.1002/qj.49712354106>, 1997.

1477

1478 Rougier, J. C., Goldstein, M. and House, L.: Second-order exchangeability analysis for multi-model  
 1479 ensembles, *Journal of the American Statistical Association*, 108, 852-863,  
 1480 [doi:10.1080/01621459.2013.802963](https://doi.org/10.1080/01621459.2013.802963), 2013.

1481

1482 Salami, M. B.: Late Cretaceous and Early Tertiary Palynofacies of Southwestern Nigeria, *Revista*  
 1483 *Espanola de Micropaleontologia*, XVI, 415-423, 1984.

1484

1485 Salard-Chebouldaeff, M.: Palynologie Maestrichtienne et Tertiaire du Cameroun. Etude qualitative et  
 1486 repartition verticale des principales especes, *Review of Palaeobotany and Palynology*, 28, 365-388,  
 1487 [https://doi.org/10.1016/0034-6667\(79\)90032-0](https://doi.org/10.1016/0034-6667(79)90032-0), 1979.

1488

1489 Salerno, J., Diem, J. E., Konecky, B. L. and Hartter, J.: Recent intensification of the seasonal rainfall  
 1490 3391 cycle in equatorial Africa revealed by farmer perceptions, satellite-based estimates, and ground-  
 1491 based station 3392 measurements, *Climatic Change*, 153(1-2):123-139, DOI:10.1007/s10584-019-  
 1492 02370-4, 2019.

1493

1494 Sepulchre, P., Caubel, A., Ladant, J.-B., Bopp, L., Boucher, O., Braconnot, P., Brockmann, P., Cozic,  
 1495 A., Donnadiou, Y., Dufresne, J.-L., Estella-Perez, V., Ethé, C., Fluteau, F., Foujols, M.-A., Gastineau,  
 1496 G., Ghattas, J., Hauglustaine, D., Hourdin, F., Kageyama, M., Khodri, M., Marti, O., Meurdesoif, Y.,  
 1497 Mignot, J., Sarr, A.-C., Servonnat, J., Swingedouw, D., Szopa, S. and Tardif, D.: IPSL-CM5A2 – an  
 1498 Earth system model designed for multi-millennial climate simulations, *Geosci. Model Dev.*, 13, 3011-  
 1499 3053, <https://doi.org/10.5194/gmd-13-3011-2020>, 2020.  
 1500  
 1501 Smagorinsky, J.: General Circulation Experiments with the Primitive Equations: I The Basic  
 1502 Experiment, *Mon. Weather Rev.*, 91, 99-164, [https://doi.org/10.1175/1520-0493\(1963\)091<0099:GCEWTP>2.3.CO;2](https://doi.org/10.1175/1520-0493(1963)091<0099:GCEWTP>2.3.CO;2), 1963.  
 1503  
 1504  
 1505 Stepanek, C. and Lohmann, G.: Modelling mid-Pliocene climate with COSMOS, *Geosci. Model Dev.*,  
 1506 5, 1221-1243, <https://doi.org/10.5194/gmd-5-1221-2012>, 2012.  
 1507  
 1508 Takata, K., Watanabe, T. and Emori, S.: Development of the minimal advanced treatments of surface  
 1509 interaction and runoff, *Global Planet. Change*, 38, 209-222, doi:10.1016/S0921-8181(03)00030-4,  
 1510 2003.  
 1511  
 1512 Tarnavsky, E., Grimes, D., Maidment, R. I., Black, E., Allan, R. P., Stringer, M., Chadwick, R. and  
 1513 Kayitakire, F.: Extension of the TAMSAT Satellite-based Rainfall Monitoring over Africa and from  
 1514 1983 to present. *J. Applied Meteor. and Climatol.*, 53(12): 2805-2822. DOI: 10.1175/JAMC-D-14-  
 1515 0016.1, 2014.  
 1516  
 1517 Taylor, K. E., Stouffer, R. J. and Meehl, G. A.: An overview of CMIP5 and the experiment design, *B.*  
 1518 *Am. Meteorol. Soc.*, 93, 485-498, <https://doi.org/10.1175/BAMS-D-11-00094.1>, 2011.  
 1519  
 1520 Tiedtke, M.: Representation of Clouds in Large-Scale Models, *Mon. Weather Rev.*, 121, 3040-3061,  
 1521 [https://doi.org/10.1175/1520-0493\(1993\)121<3040:ROCILS>2.0.CO;2](https://doi.org/10.1175/1520-0493(1993)121<3040:ROCILS>2.0.CO;2), 1993.  
 1522  
 1523 Tierney, J. E., Poulsen, C. J., Montañez, I. P., Bhattacharya, T., Feng, R., Ford, H. L., Hönlisch, B.,  
 1524 Inglis, G. N., Petersen, S. V., Sahoo, N., Tabor, C. R., Thirumalai, K., Zhu, J., Burls, N. J., Foster, G.  
 1525 L., Goddérís, Y., Huber, B. T., Ivany, L. C., Turner, S. K., Lunt, D. J., McElwain, J. C., Mills, B. J.  
 1526 W., Otto-Bliesner, B. L., Ridgwell, A. and Zhang, Y.-G.: Past climates inform our future, *Science*,  
 1527 370 (6510), DOI: 10.1126/science.aay3701, 2020.  
 1528

1529 Tokioka, T., Yamazaki, K., Kitoh, A. and Ose, T.: The Equatorial 30-60 day Oscillation and the  
 1530 Arakawa-Schubert Penetrative Cumulus Parameterization, *J. Meteorol. Soc. Japan*, 66, 883-901,  
 1531 [https://doi.org/10.2151/jmsj1965.66.6\\_883](https://doi.org/10.2151/jmsj1965.66.6_883), 1988.

1532

1533 Utescher, T., Bruch, A. A., Erdei, B., François, L., Ivanov, D., Jacques, F. M. B., Kern, A. K., Liu,  
 1534 Y.-S., Mosbrugger, V. and Spicer, R. A.: The Coexistence Approach - Theoretical background and  
 1535 practical considerations of using plant fossils for climate quantification, *Palaeogeography,*  
 1536 *Palaeoclimatology, Palaeoecology*, 410, 58-73, <https://doi.org/10.1016/j.palaeo.2014.05.031>, 2014.

1537

1538 Utescher, T. and Mosbrugger, V.: Eocene vegetation patterns reconstructed from plant diversity – A  
 1539 global perspective, *Palaeogeogr. Palaeocl.*, 247, 243–271, doi:10.1016/j.palaeo.2006.10.022, 2007.

1540

1541 Uzodimma, D. E.: Palynostratigraphy, Age Determination and Depositional Environments of the Imo  
 1542 Shale Exposures at the Okigwe/Port Harcourt Express Road Junction Okigwe, Southeastern Nigeria,  
 1543 *Greener Journal of Physical Sciences*, 3, 255-272, ISSN: 2276-7851, 2013.

1544

1545 van Dijk, J., Fernandez, A., Bernasconi, S. M., Caves Rugenstein, J. K., Passey, S. R. and White, T.:  
 1546 Spatial pattern of super-greenhouse warmth controlled by elevated specific humidity, *Nat. Geosci.*,  
 1547 13, 739–744, <https://doi.org/10.1038/s41561-020-00648-2>, 2020.

1548

1549 Valdes, P. J., Armstrong, E., Badger, M. P. S., Bradshaw, C. D., Bragg, F., Crucifix, M., Davies-  
 1550 Barnard, T., Day, J. J., Farnsworth, A., Gordon, C., Hopcroft, P. O., Kennedy, A. T., Lord, N. S.,  
 1551 Lunt, D. J., Marzocchi, A., Parry, L. M., Pope, V., Roberts, W. H. G., Stone, E. J., Tourte, G. J. L. and  
 1552 Williams, J. H. T.: The BRIDGE HadCM3 family of climate models: HadCM3@Bristol v1.0, *Geosci.*  
 1553 *Model Dev.*, 10, 3715-3743, <https://doi.org/10.5194/gmd-10-3715-2017>, 2017.

1554

1555 Volodin, E. M. and Lykossov, V. N.: Parameterization of Heat and Moisture Transfer in the Soil-  
 1556 Vegetation System for Use in Atmospheric General Circulation Models: 2. Numerical Experiments in  
 1557 Climate Modeling, *Izvestiya Atmospheric and Oceanic Physics*, 34(5), 559-569, 1998.

1558

1559 Volodin, E. M., Mortikov, E. V., Kostykin, S. V., Galin, V. Y., Lykossov, V. N., Gritsun, A. S.,  
 1560 Diansky, N. A., Gusev, A. V. and Iakovlev, N. G.: Simulation of the present-day climate with the  
 1561 climate model INMCM5, *Clim. Dynam.*, 49, 3715-3734, 10.1007/s00382-017-3539-7, 2017.

1562

1563 Volodin, E. M., Mortikov, E. V., Kostykin, S. V., Galin, V. Y., Lykossov, V. N., Gritsun, A. S.,  
 1564 Diansky, N. A., Gusev, A. V., Iakovlev, N. G., Shestakova, A. A. and Emelina, S. V.: Simulation of  
 1565 the modern climate using the INMCM48 climate model, *Russ. J. Numer. Anal. M.*, 33, 367-374,



<https://doi.org/10.1515/rnam-2018-0032>, 2018.

West, C. K., Greenwood, D. R., Reichgelt, T., Lowe, A. J., Vachon, J. M., and Basinger, J. F.: Paleobotanical proxies for early Eocene climates and ecosystems in northern North America from middle to high latitudes, *Clim. Past*, 16, 1387-1410, <https://doi.org/10.5194/cp-16-1387-2020>, 2020.

Westerhold, T., Marwan, N., Drury, A. J., Liebrand, D., Agnini, C., Anagnostou, E., Barnet, J. S. K., Bohaty, S. M., De Vleeschouwer, D., Florindo, F., Frederichs, T., Hodell, D. A., Holbourn, A. E., Kroon, D., Lauretano, V., Littler, K., Lourens, L. J., Lyle, M., Pälike, H., Röhl, U., Tian, J., Wilkens, R. H., Wilson, P. A. and Zachos, J. C.: An astronomically dated record of Earth's climate and its predictability over the last 66 million years, *Science*, 369(6509), 1383-1387, <https://doi.org/10.1126/science.aba6853>, 2020.

Wilf, P., Wing, S. L., Greenwood, D. R. and Greenwood, C. L.: Using fossil leaves as paleoprecipitation indicators: An Eocene example, *Geology*, 26, 203-206, [https://doi.org/10.1130/0091-7613\(1998\)026<0203:UFLAPI>2.3.CO;2](https://doi.org/10.1130/0091-7613(1998)026<0203:UFLAPI>2.3.CO;2), 1998.

Williams, C. J. R.: Paleobotanical precipitation estimates used in Williams et al.: African hydroclimate monsoon during the early Eocene from the DeepMIP simulations, *Paleoceanography and Paleoclimatology*, 2022, (Version 1) [Dataset], Zenodo, DOI: 10.5281/zenodo.6472914, 2022.

Williams, C. J. R., Guarino, M.-V., Capron, E., Malmierca-Vallet, I., Singarayer, J. S., Sime, L. C., Lunt, D. J. and Valdes, P. J.: CMIP6/PMIP4 simulations of the mid-Holocene and Last Interglacial using HadGEM3: comparison to the pre-industrial era, previous model versions and proxy data, *Clim. Past*, 16, 1429-1450, <https://doi.org/10.5194/cp-16-1429-2020>, 2020.

Williams, C. J. R. and Kniveton, D. R. (eds). *African Climate and Climate Change: Physical, Social and Political Perspectives*. Springer Science+Business Media BV 2011. Dordrecht, Heidelberg, London and New York: 212pp. DOI: 10.1007/978-90-481-3842-5, 2011.

Williams, C. J. R., Kniveton, D. R. and Layberry, R.: Climatic and oceanic associations with daily rainfall extremes over southern Africa, *Int. J. Clim.*, 27 (1): 93-108, <https://doi.org/10.1002/joc.1376>, 2007.

Williams, C. J. R., Kniveton, D. R. and Layberry, R.: Influence of South Atlantic sea surface temperatures on rainfall variability and extremes over southern Africa, *J. Clim.*, 21: 6498-6520, DOI: <https://doi.org/10.1175/2008JCLI2234.1>, 2008.

1603  
1604 Williams, C. J. R., Kniveton, D. R. and Layberry, R.: Assessment of a climate model to reproduce  
1605 rainfall variability and extremes over southern Africa, *Theor. Applied Climatol.*, 99: 9-27, DOI:  
1606 10.1007/s00704-009-0124-y, 2010.  
1607  
1608 Williams, C. J. R., Sellar, A. A., Ren, X., Haywood, A. M., Hopcroft, P., Hunter, S. J., Roberts, W. H.  
1609 G., Smith, R. S., Stone, E. J., Tindall, J. C., and Lunt, D. J.: Simulation of the mid-Pliocene Warm  
1610 Period using HadGEM3: experimental design and results from model–model and model–data  
1611 comparison, *Clim. Past*, 17, 2139-2163, <https://doi.org/10.5194/cp-17-2139-2021>, 2021.  
1612  
1613 Willard, D. A., Donders, T. H., Reichgelt, T., Greenwood, D. R., Sangiorgi, F., Peterse, F., Nierop, K.  
1614 G. J., Frieling, J., Schouten, S. and Sluijs, A.: Arctic vegetation, temperature, and hydrology during  
1615 Early Eocene transient global warming events, *Global and Planetary Change*, 178, 139-152,  
1616 <https://doi.org/10.1016/j.gloplacha.2019.04.012>, 2019.  
1617  
1618 Wright, I. J., Dong, N., Maire, V., Prentice, I. C., Westoby, M., Díaz, S., Gallagher, R. V., Jacobs, B.  
1619 F., Kooyman, R., Law, E. A., Leishman, M. R., Niinemets, U., Reich, P. B., Sack, L., Villar, R.,  
1620 Wang, H. and Wilf, P.: Global climatic drivers of leaf size, *Science*, 357(6354), 917–921, DOI:  
1621 10.1126/science.aal4760, 2017.  
1622  
1623 Xie, Y. L., Wu, F. L. and Fang, X. M.: Middle Eocene East Asian monsoon prevalence over southern  
1624 China: Evidence from palynological records, *Global and Planetary Change*, 175, 13-26, DOI:  
1625 10.1016/j.gloplacha.2019.01.019, 2019.  
1626  
1627 Zhang, G. J. and McFarlane, N. A.: Sensitivity of climate simulations to the parameterization of  
1628 cumulus convection in the Canadian Climate Centre general circulation model, *Atmosphere–Ocean*,  
1629 33(3), 407-446, <https://doi.org/10.1080/07055900.1995.9649539>, 1995.  
1630  
1631 Zhang, M., Lin, W., Bretherton, C. S., Hack, J. J. and Rasch, P. J.: A modified formulation of  
1632 fractional stratiform condensation rate in the NCAR Community Atmospheric Model (CAM2), *J.*  
1633 *Geophys. Res.*, 108(D1), 4035, <https://doi.org/10.1029/2002JD002523>, 2003.  
1634  
1635 Zhu, J., Poulsen, C. J. and Otto-Bliesner, B. L.: High climate sensitivity in CMIP6 model not  
1636 supported by paleoclimate, *Nat. Clim. Chang*, 10, 378-379, [https://doi.org/10.1038/s41558-020-0764-](https://doi.org/10.1038/s41558-020-0764-6)  
1637 6, 2020.  
1638  
1639

